Applied Geochemistry 193 (2025) 106564

Contents lists available at ScienceDirect

Applied Geochemistry

journal homepage: www.elsevier.com/locate/apgeochem

# Radiocarbon age dating and quality evolution of seawater intruding beneath a freshwater lens

Pieter J. Stuyfzand [a,b,*], Philip R. Nienhuis [c,1], Vincent E.A. Post [d]

[a] CEG, Delft University of Technology, Delft, Netherlands
[b] Stuyfzand Hydroconsult+, Brederodestraat 138, 2042 BL, Zandvoort, Netherlands
[c] Waternet, P.O.Box 94370, 1090 GJ, Amsterdam, Netherlands
[d] Edinsi Groundwater, Amsterdam, Netherlands

ARTICLE INFO

Editorial Handling by: Ding He

*Keywords:*
Radiocarbon age dating
Saltwater intrusion
Multitracing
Mass balancing
Hydrogeochemical processes
Palaeohydrology

ABSTRACT

Radiocarbon has been used in a number of studies to establish the age of intruded seawater, yet there appears to be a paucity of investigations that has attempted to quantify the processes that influence radiocarbon along the flow path of actively intruding seawater. The present study contributes to filling this research gap using radiocarbon and hydrochemical data of intruding North Sea water along two shore-perpendicular transects across the coastal dune belt of the western Netherlands. The objective is to establish how well radiocarbon can be used to determine the intruding seawater's age, considering the corrections that are required to account for geochemical reactions and mixing.

The effect of geochemical reactions was quantified for each of the 18 samples of intruded seawater based on a chemical mass balance calculated with a new Excel based code (R + SWi). It considers 20 quality parameters (including $\delta^{13}C_{DIC}$ and $^{14}C_{DIC}$) and 15 reactions and utilizes Excel's Solver routine to calibrate the model parameters. The reactions along the flow path are initially dominated by $O_2$ and $NO_3$ reduction by sediment organic matter in seafloor sediment, with little $CaCO_3$ dissolution. Next, during passage of a Holocene tidal aquitard, Fe $(OH)_3$ and some $SO_4$ are reduced, pyrite and $CaCO_3$ precipitate, and opaline $SiO_2$ dissolves. In deeper, Pleistocene aquitards and further downgradient in aquifers, cations are exchanged, some $CaCO_3$ precipitates due to Ca exchange, and siderite dissolves.

Correcting radiocarbon concentrations for the calculated sedimentary carbon contributions yields ages between 0.37 and 6 ka. Sensitivity analysis reveals that the corrected $^{14}C$ age is most sensitive to the assumed $^{14}C$ activity of the carbonate and organic matter of the Holocene seabed sediments. The intruded seawater's age appears to be bimodal: Old seawater (3–6 ka) intruded when the coastline was located much further to the east than at present. Younger seawater (<3 ka) started to intrude after the freshwater lens developed when the coastline had reached its present-day position. Groundwater extraction and especially the reclamation of the Haarlemmermeer lake accelerated intrusion rates massively.

The results of a 3.5 ky numerical model simulation of freshwater lens formation and seawater intrusion are consistent with the radiocarbon age pattern inferred from the samples. The spatial distribution of seawater ages indicates a higher vulnerability to salinization in the northern part of the study area, highlighting the added value of radiocarbon data of saline groundwater for water resource management purposes.

List of frequently used abbreviations

| Abbreviation | Explanation |
|---|---|
| $^{14}C_{M,COR}$ | measured $^{14}C$ corrected for admixed deep dune groundwater |

(*continued on next column*)

(*continued*)

| Abbreviation | Explanation |
|---|---|
| $^{14}C_{ND}$ | calculated $^{14}C$ activity of DIC, without decay and admixing, with diluting effects of carbonate dissolution and SOM oxidation |

(*continued on next page*)

* Corresponding author. CEG, Delft University of Technology, Delft, Netherlands.
*E-mail address:* p.j.stuijfzand@tudelft.nl (P.J. Stuyfzand).
[1] retired.

https://doi.org/10.1016/j.apgeochem.2025.106564
Received 16 April 2025; Received in revised form 5 July 2025; Accepted 8 September 2025
Available online 17 September 2025

(*continued*)

| Abbreviation | Explanation |
|---|---|
| AD | Anno Domini (year 0) |
| AR | Artificial Recharge (zone) |
| ASL | Above Sea Level |
| AtOc | Atlantic Ocean Water |
| BAR | Basin Artificial Recharge |
| BC | Before Christ (years before 0) |
| BEX | Base Exchange Index |
| BP | Before Present |
| BSL | Below Sea Level |
| CMB | Chemical Mass Balance |
| CNS | Coastal North Sea Water |
| DIC | Dissolved Inorganic Carbon |
| DOC | Dissolved Organic Carbon |
| EC | Electrical Conductivity |
| $f_D$, $f_O$, $f_R$ | dune, ocean and river water fraction in 'intruded' CNS |
| HWL | North Sea High Water Line |
| ka | 1000 years |
| pmC | Percent Modern Carbon |
| R + Swi | Code Reactions + to calculate CMB for Salt Water Intrusion, set in Excel |
| $SI_M$ | Saturation Index for Mineral 'M' |
| SOM | Sediment Organic Matter |
| TDS | Total Dissolved Solids |
| TEs | Trace Elements |
| TU | Tritium Units |
| V-SMOV | Vienna Standard Mean Ocean Water |

## 1. Introduction

Seawater intrusion threatens coastal groundwater resources worldwide (Jiao and Post, 2019; Werner et al., 2013). Besides groundwater extraction, there can be other causes that cause seawater intrusion, such as lowering of water levels by land reclamation or sea level rise. The salinity of groundwater in coastal areas is often a reflection of past processes, some of which have occurred thousands of years ago. An understanding of coastal groundwater ages is therefore important as it assists in identifying the processes that led to salinization.

Yechieli et al. (2001) stated that age dating of saline groundwater in coastal aquifers has received relatively little attention. To date this still appears to be true, with a few notable exceptions. In the coastal aquifer system of Israel Yechieli et al. (2009) sampled fresh- and saline groundwater and found that the age of the deepest saline groundwater was 6–12 ky. The fact that waters were progressively younger with decreasing depth was linked to the effect of the rise of the Mediterranean sea level during the Holocene. More detailed analysis of $^{3}H$ and $^{14}C$ vertical profiles across the fresh-saltwater interface in the shallowest aquifer showed intrusion of seawater 15–40 years prior to sampling (Sivan et al., 2005). The relatively low (60 pMC) values of $^{14}C$ were attributed to oxidation of $^{14}C$-free organic carbon. Yechieli et al. (2019) inferred from a suite of tracers, including $^{14}C$, $^{39}Ar$ and $^{81}Kr$, that ~1 km deep saline groundwater, previously believed to be millions of years old, must be younger than 40 ka.

Haseguwa et al. (2023) also used multiple isotope tracers ($^{4}He$, $^{14}C$, $^{36}Cl$ and $^{37}Cl$) to establish the sources of groundwater on the Miura Peninsula (Japan). Their data allowed them to distinguish between modern seawater in the permeable sandstone and fossil seawater in the low-permeability mudstones at greater depth. Lee et al. (2016) used radiocarbon ($^{14}C$) to estimate the age of saline groundwater near Melbourne (Australia) and found that it was marine groundwater trapped during the mid-Holocene sea level highstand. A study in a nearby area also found marine water with a relic origin, which was inferred from multiple tracers including radiocarbon, although ages were not calculated (Currell et al., 2015).

Dang et al. (2022) found brine in sediments of the Luanhe River delta (China) that, based on its radiocarbon activity, was attributed to seawater evaporation in a lagoon in the period 7–3.5 ka BP. Similarly, in southern Spain, Sola et al. (2025) identified brines formed in an ancient lagoon in conjunction with intruded seawater. They proposed that age-dated coastal groundwaters could be a tool complementary to sedimentological records to reconstruct the Holocene coastline evolution. To what extent radiocarbon was influenced by flow and mixing processes was however not quantified.

While these studies have demonstrated how radiocarbon can be used to estimate ages of saline groundwater in coastal aquifer systems, there is still a need for investigations of the processes affecting radiocarbon along a well-defined flow path of intruding seawater. The main reasons for the lack of previous work, besides the fact that $^{14}C$-age dating is complex (Clark and Fritz, 1997; Plummer and Glynn, 2013), are that the expected travel times are often relatively short (<50 years) which makes $^{14}C$ not the age-tracer of first choice. Moreover groundwater monitoring networks rarely target the saline parts of the aquifer system, hence suitable observation wells tend to be limited in number. To address this research gap, the present paper investigates the age distribution and hydrochemical evolution of intruded North Sea water flowing in a deep (>200 m) leaky aquifer system below a thick (>100 m) fresh dune water lens (Figs. 1 and 2). The objective is to establish how well radiocarbon can be used to determine the intruding seawater's age, given the corrections that are required to account for geochemical reactions and mixing.

The area is uniquely suited for this study. A dense network of multilevel observation wells with short (1–2 m) well screens is located at depths ranging from sea level to 100–200 m below sea level (BSL). In addition, the history of groundwater extraction from the coastal dune area has been well documented, data on the hydrogeological structure, groundwater levels, salinity and water quality are abundant. As a result, the flow patterns (Kamps et al., 2005; Delsman et al., 2014) and the geochemical reactions that interfere with radiocarbon age determination are well understood (Stuyfzand, 1993a, 1993b).

This paper builds on these earlier studies, which lack radiocarbon data and data on various trace elements. It demonstrates the corrections needed to take into account the geochemical reactions between the intruding seawater and sedimentary carbon sources. A numerical groundwater model that simulates the palaeohydrological evolution of the coastal area is used to validate ages inferred from the radiocarbon data.

## 2. Material and methods

### 2.1. Study area

The 4–5 km wide coastal dune area is situated south of Zandvoort (Fig. 1), about 25 km west of Amsterdam, The Netherlands. About 36 $km^2$ of these dunes comprise the main drinking water catchment area of the city of Amsterdam. The extraction of dune groundwater started in 1853, and basin artificial recharge (BAR) with pretreated Rhine River water has been applied since 1957 to halt and reverse the lateral intrusion and upconing of intruded North Sea water. To the east of the dune belt lies the former Lake Haarlemmermeer (206 $km^2$) It was reclaimed in 1849–1852 and has been a deep (approximately 5 m BSL) polder ever since. Its western border is situated 3–4 km from the dune area, and 7–9 km from the North Sea shore.

### 2.2. Spatial distribution of hydrosomes

In the study area, 6 hydrosomes (waterbodies with a specific origin; Stuyfzand et al., 2011) coexist (Fig. 2), from ancient to young: brackish to saline palaeogroundwater upconing from marine clay and sand deposits of Early Pleistocene and Late Tertiary age (M); relict, saline Holocene transgression water (hard to discern from S), which infiltrated in an open, sandy marine environment with little protection from coastal barriers (L/S); coastal North Sea water which infiltrated offshore (S); relict, brackish Holocene transgression water which infiltrated behind

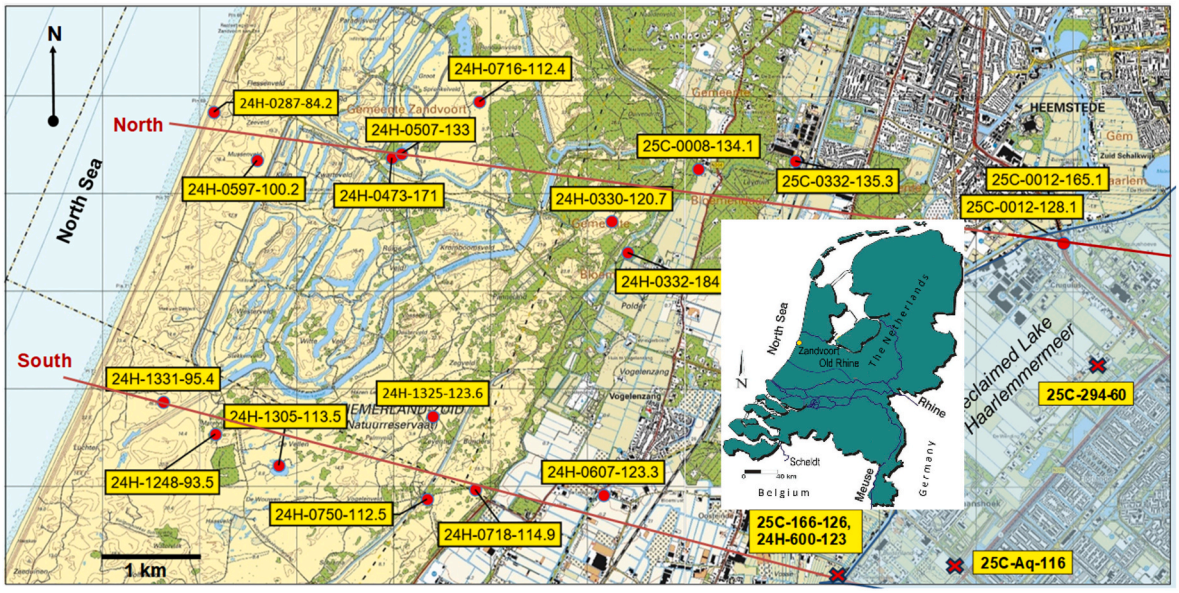


**Fig. 1.** Location map with the position of transects 'north' and 'south', and the sampled monitoring wells (red dots). Red cross = well without isotope analyses, sampled in past and projected onto transect. Well code: sheet No. of topographical map (24H or 25C), well No. on sheet (e.g. 1331) and screen depth (e.g. 95.4 m below sea level). (For interpretation of the references to color in this figure legend, the reader is referred to the Web version of this article.)

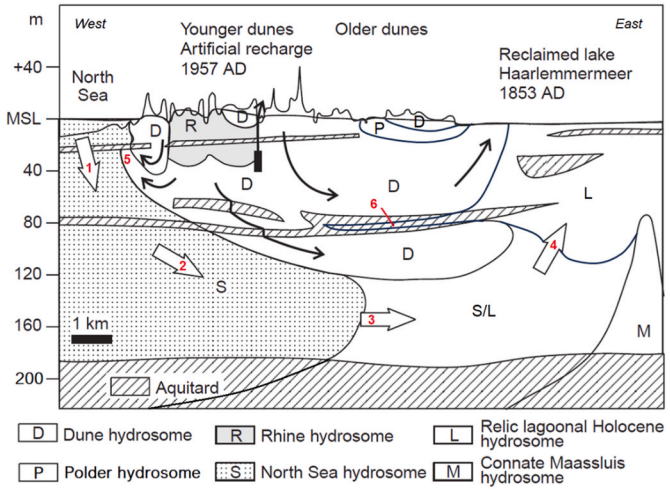


**Fig. 2.** Schematic cross section along transect north, slightly extended inland, showing the spatial distribution of the main aquitards as well as hydrosomes (Modified from Stuyfzand et al., 2011). S/L = gradual transition from S to L; 1–4 = studied flow path; 5 = freshwater tongue under sea floor; 6 = Cl inversion. The data used to map the hydrosomes were collected during the period 1975–1990.

coastal barriers in a lagoonal, marsh environment underlain by peat (L); fresh dune groundwater (D); fresh to slightly brackish polder water (P) consisting of a mixture of dune groundwater, Rhine River water and exfiltrated Holocene transgression water; and fresh, pretreated Rhine River water (R), which is artificially recharged via basins. Their spatial distribution as shown in Fig. 2 was mapped with the following tracers: EC, Cl, Cl/Br, $SO_4$, $HCO_3$, $^3H$ and $\delta^{18}O$ (Stuyfzand, 1993b, 1999). The focus of this study is on hydrosomes S and S/L.

### 2.3. The aquifer system

The aquifer system down to 180 m BSL consists of 5 sandy aquifers (1–5) and 7 aquitards (A-G) (Fig. 3, Table 1). It is uncertain how far the aquitards extend below the sea floor, and where there are any aquitard windows (Stuyfzand, 1988 demonstrated gaps on land). There is a general northward dip of the discerned hydrogeological units. The sampled piezometers are screened in semiconfined aquifer 3 (n = 11), aquifer 3A in the south (n = 5), and aquifer 5 in the north (n = 2); see Fig. 3. These aquifers are of Early Pleistocene age and are composed of unconsolidated coarse sands ($d_{50}$ 300–450 μm) with some gravel. They are poor in reactive solid phases (Table 1).

The observed patterns in water quality and age distribution along both flow paths can only be explained with this (paleo)hydrological record in mind. The aquifer system experienced 10 hydrological stress periods since ca. 8.5 ka BP (Table 2). These periods are associated with the Holocene transgression, followed by coastal progradation and the shift of fluvial outlets, coastal regression, dune and peat formation, and anthropogenic changes by peat excavation, reclamation of inland lakes, groundwater extraction and artificial recharge.

### 2.4. Sampling and analysis

Samples of saline groundwater were collected along 2 transects in December 2019 and March 2022. Eighteen piezometers screened at 84–183 m BSL, and located between 45 and 8610 m from the North Sea High Water Line (HWL) were sampled (Fig. 1). The samples were taken twice, because of problems with the chemical analysis in the laboratory. Each piezometer is nested in a multi-piezometer borehole composed of 5–13 piezometers at different depths, each with a 1–2 m long well screen and riser diameter of 2.5–5 cm. Clay seals in between well screens prevent vertical leakage inside the boreholes.

The piezometers were purged using a high capacity pump, removing at least three times their standing water volume until EC and temperature readings became stable. After purging the pumping rate was reduced and pH, EC, $O_2$ and temperature were measured on site in a flow-through cell. Subsequently the samples for analysis at the Waterlaboratorium (Haarlem, The Netherlands) were taken. Samples for an ICP-MS multi-scan analysis of cations, $PO_4$, $SiO_2$ and trace elements were filtrated in the field over 0.45 μm and acidified with ultrapure $HNO_3$ (60 %, 0.7 mL/100 cc). Samples for ion chromatographic analysis of Cl, Br, $SO_4$, $NO_3$, and F and for acid titration of alkalinity were not filtrated and not acidified but analyzed within 24 h in the lab. Samples for $NH_4$ and TOC (both unfiltered) were analyzed by spectrophotometry and by chemical-based oxidation, respectively. The high salinity of each

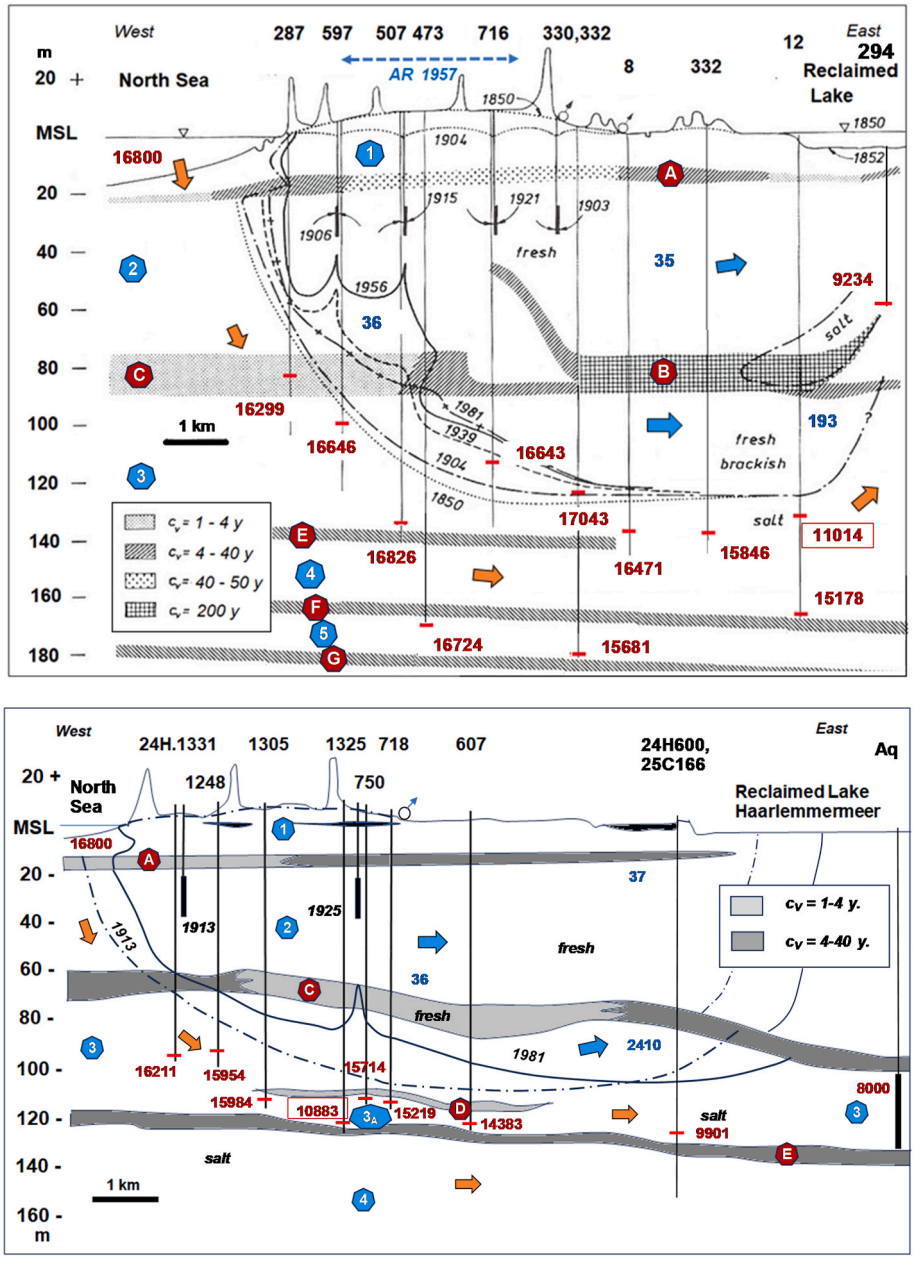


**Fig. 3.** Schematic of transect north (top) and south (bottom), showing the position of sampled piezometers (red cross line) with their Cl concentration in red (mg/L), aquifers (1–5), aquitards (A–G), fresh-salt interface (8400 mg Cl/L) for successive years, water table and important hydrological changes. 1850 = background situation prior to reclamation of lake in 1852 and start groundwater extraction in 1853; 1904–1913 = before large scale addition of deep wells in period 1903–1925; 1956 = year before artificial recharge started in northern area (AR). Location of transects in Fig. 1 $c_V$ = vertical hydraulic resistance of aquitards [year]. Blue numbers = Cl dune groundwater in aquifer 2. The framed red numbers indicate substantial admixing of fresh dune groundwater (ca. 35 %). (For interpretation of the references to color in this figure legend, the reader is referred to the Web version of this article.)

sample (on average 30,000 mg/L) necessitated a 10–100 fold dilution step, except for total alkalinity, $NH_4$ and DOC.

The estimated precision of most analyzed main constituents is indicated in Table 4 as a percentage of the measured value. For instance, 1.8 % for Cl = 16,000 mg/L yields a range between 15,700 and 16,300 mg/L, assuming the error to be two-sided and symmetrical. This precision (Pr) includes, in addition to analytical precision, the effects of sampling, dilution prior to analysis and minor changes over time (2.25 years between first and second sampling round) at screen depth in the aquifer. It was calculated as follows from the 18 samples taken in 2019 ($C_A$) and 2022 ($C_B$):

$$\mathrm{Pr} = 200\frac{\sum_{i=1}^{i=18}|C_{A,i} - C_{B,i}|}{\sum_{i=1}^{i=18}(C_{A,i} + C_{B,i})} \quad (1)$$

In a similar way, the precision of the trace elements B, Ba, Mo, Rb, Sr and V was estimated (Table 5). For the remaining main constituents and trace elements precision could not be established due to lack of repeat analysis between the first and second sampling, or due to analytical problems.

All data were checked by the charge balance, relation between measured and calculated EC, redox consistency (e.g. no $O_2$ in high $NH_4$

**Table 1**
Geological, hydrological and geochemical characteristics of aquifers (1–5) and aquitards (A-G) in the study area (discerned in Fig. 3). Strongly modified after Stuyfzand (1993b). Both investigated flow paths pass subsequently 1, A, 2, C and 3, the southern also D and IIIB, and the northern also E, 4, F and 5.

| No. | Hydrogeological units | Geology | Depth | $K_h$ or | $d_{50}$ | poro- | %Clay | $C_{ORG}$ | CEC | $CaCO_3$ | $FeS_2$ |
|---|---|---|---|---|---|---|---|---|---|---|---|
| | (see Fig. 2 for position) | Chronostratigr.: Geol. Formation # | m BSL | $c_V$ | µm | sity | <2 µm | % | meq/kg | % | ppm |
| AQUIFERS | | | | $K_h$ [m/d] | | | | | | | |
| 1 | Dune sand on top of beach and shallow marine sand | Holocene: Naaldwijk | −5 to 13 | 15 | 250 | 40 | 0.7 | 0.15 | 12 | 5 | <10 |
| 2 | Aeolian, marine and fluvial sands | L/M. Pleistocene: Kr, Eemian, U&S | 19 to 60 | 25 | 300 | 38 | 1 | 0.20 | 15 | 3 | 200 |
| 3 | Fluvial coarse sand with some gravel | M/E. Pleistocene: Waalre Peize | 80 to 120 | 45 | 400 | 35 | 0.7 | 0.05 | 4 | <0.3 | 50 |
| 3B | Fluvial coarse sand with some gravel | E. Pleistocene: Peize | 112 to 120 | 40 | 350 | 34 | 2 | 0.10 | 5 | 0.3 | 50 |
| 4 | Fluvial coarse sand with some gravel | E. Pleistocene: Peize | 125 to 170 | 35 | 325 | 33 | 1 | 0.05 | 4 | 0.3 | 50 |
| 5 | Fluvial coarse sand with some gravel | E. Pleistocene: Peize | 165 to 180 | 30 | 300 | 32 | 2 | 0.10 | 7 | 1 | 100 |
| AQUITARDS | | | | $c_V$ [yr] | | | | | | | |
| A | Very fine sandy clay, sea floor and tidal flat deposits | Holocene: Naaldwijk | 13 to 19 | 1–50 | 100 | 35 | 5–20 | 3 | 20–100 | 10 | 500 |
| B | Boulder clay and glaciolimnic clay | L. Pleistocene: Drenthe | 60 to 78 | 4–200 | 16–500 | 20 | 15–35 | 1 | 85 | 3 | 250 |
| C | Fluvial clay loam with (some) peat | M/E. Pleistocene: Waalre | 60 to 80 | 1–40 | 60 | 30 | 10 | 5 | 140 | 12 $ | 500 |
| D | Fluvial clay loam | E. Pleistocene: Peize | 110 to 112 | 1–4 | 60 | 28 | 10 | 2 | 100 | 1 | 250 |
| E | Fluvial clay loam with (some) peat | E. Pleistocene: Peize | 120 to 125 | 4–40 | 60 | 29 | 10 | 5 | 140 | 1 | 750 |
| F | Fluvial clay loam | E. Pleistocene: Peize | 165 to 170 | 4–40 | 100 | 27 | 5–20 | 3 | 20–100 | 10 | 300 |
| G | Marine silty sand and clay | E. Pleistocene: Maassluis | 180 to 350 | 4–40 | 100 | 27 | 5–20 | 3 | 20–100 | 10 | 1000 |

#: E = Early; L = Late; M = Middle; Kr = Kreftenheye; U&S = Urk & Sterksel.
$: also containing manganous siderite nodules.

**Table 2**
Definition and description of 10 hydrological stress periods since 8.5 ka BP. Modified from Delsman et al. (2014). Peat elev = Top elevation of former peat surface behind dune barriers; $BSL_C$ = Below current Sea Level; ASL = Above Sea Level back then; BAR = Basin Artificial Recharge.

| Period | | | | Sea Level | | Coastal dune | Peat elev. | Description of special event |
|---|---|---|---|---|---|---|---|---|
| Start | | End | | m $BSL_C$ | | ridge(s) | m ASL | |
| 6500 | BC | 4500 | BC | 22 | 8 | none preserved | 0 | Max. inland extent of Holocene transgression |
| 4500 | BC | 3300 | BC | 8 | 5 | | 0.1 | Open coastline, deposition marine clay + sand |
| 3300 | BC | 2100 | BC | 5 | 3.5 | # | 0.5 | 2600 BC: Old Rhine became main Rhine outlet |
| 2100 | BC | 700 | BC | 3.5 | 2 | | 1 | |
| 700 | AD | 500 | AD | 2 | 1 | | 1.5 | |
| 500 | AD | 1500 | AD | 1 | 0.9 | $ | 2 | 850 AD: Old Rhine mouth silting up; 1300 AD: younger dunes reached max. inland position |
| 1500 | AD | 1850 | AD | 0.9 | 0.3 | Little changes in position dune ridges | 0 | Rapid peat degradation by drainage, peat digging/removal, formation of lakes behind dunes |
| 1850 | AD | 1900 | AD | 0.3 | 0.1 | | 0 | 1852: reclamation of Lake Haarlemmermeer, 1853: abstraction of shallow dune groundwater starting |
| 1900 | AD | 1957 | AD | 0.1 | 0.05 | | 0 | 1904: rapid expansion dune groundwater extraction by deep wells, leading to lateral North Sea intrusion + upconing |
| 1957 | AD | – | AD | 0.05 | 0 | | 0 | 1957: reduction extraction dune groundwater, start BAR |

#: Formation of several beach barriers with older dunes on top in period 2500 - 1000 BC.
$: Coastal erosion predominant as of 850 AD. Younger dunes formed in period 1000 - 1300 AD, overrunning several beach barriers and beach plains. Strong expansion of fresh dune groundwater lens.

groundwater) and outliers. In addition, all samples were compared with (i) the results of regular Cl monitoring (in the period 1905–1990 on an annual basis, later every 5 years), and (ii) for 7 samples, earlier hydrochemical data (period 1904–1987) reported by Stuyfzand (1988, 1993b). In order to obtain a neutral charge balance, needed for mass balancing (next section), the main cations have been multiplied with $f_C = \Sigma A/\Sigma C$ (meq sum of Anions and Cations, respectively). The higher precision of the anions justified this unidirectional adjustment, with $f_C$ varying between 0.98 and 1.08. The Excel based program HGC (Hydrogeochemcal 3.1; Stuyfzand, 2012) was used to perform calculations of e.g. EC (from dissolved main constituents), various mineral equilibria and the conversion of measured total alkalinity into carbonate alkalinity, DIC (Dissolved Inorganic Carbon) and its speciation.

Samples for isotopes were not filtrated. Untreated samples for $^2H$ and $^{18}O$ were stored in watertight, fully filled glass containers and analyzed at the Centre for Isotope Research Groningen (CIO, Netherlands), by mass spectrometry of (i) $H_2$ gas obtained from the water sample by reduction, and (ii) $CO_2$ equilibrated with water sample, respectively.

**Table 3**
The 15 reactions addressed in the chemical mass balance (R + SWI), of which reactions 14 and 15 are irrelevant in this study. The reaction numbers 1–11 are included in the $^{13}C$ balance, the species in red are primary reaction indicators. For reactions 2–7 with SOM including N and P, see A1.

| Reaction | | | | |
|---|---|---|---|---|
| No. | Select | Description | Stoichiometry | |
| 1 | X | Addition or loss of $CO_2$ | $CO_2$ losses (negative, in output) or gains (positive, in input) | |
| 2 | X | $O_2$-reduction by SOM | $O_2 + CH_2O$ à $CO_2 + H_2O$ | Ω |
| 3 | X | $NO_3$-reduction by SOM | $4\ NO_3^- + 5CH_2O$ à $2N_2 + CO_2 + 4HCO_3^- + 3H_2O$ | Ω |
| 4 | X | $SO_4$ reduction ($FeS_2$) by SOM | $2\ SO_4^{2-} + 3.5CH_2O + Fe^{2+}$ à $FeS_2 + 2HCO_3^- + 1.5CO_2 + 2.5H_2O$ | Ω |
| 5 | X | $CH_4$-formation from SOM | $CO_2 + 2CH_2O$ à $CH_4 + 2CO_2$ | Ω |
| 6 | X | $MnO_2$ reduction by SOM | $MnO_2 + 0.5CH_2O + 1.5CO_2 + 0.5H_2O$ à $Mn^{2+} + 2HCO_3^-$ | Ω |
| 7 | X | $Fe(OH)_3$ reduction by SOM | $Fe(OH)_3 + 0.25CH_2O + 1.75CO_2$ à $Fe^{2+} + 2HCO_3^- + 0.75H_2O$ | Ω |
| 8 | X | Calcite/dolomite dissolution by $CO_2$ | $Ca_{1-x}Mg_xCO_3 + CO_2 + H_2O$ à $(1-x)\ Ca^{2+} + x\ Mg^{2+} + 2\ HCO_3^-$ | $ |
| 9 | X | Siderite dissolution by $CO_2$ | $Fe_{1-y}Mn_yCO_3 + CO_2 + H_2O$ à $(1-y)\ Fe^{2+} + y\ Mn^{2+} + 2\ HCO_3^-$ | $ |
| 10 | X | Calcite/dolomite precipitation | $Ca_{1-x}Mg_xCO_3 + CO_2 + H_2O$ ß $(1-x)\ Ca^{2+} + x\ Mg^{2+} + 2\ HCO_3^-$ | $ |
| 11 | X | Proton buffering | $H\text{-}X + ½Ca^{2+} + HCO_3^-$ à $½Ca\text{-}X + CO_2 + H_2O$ | |
| 12 | X | Opal dissolution | $SiO_2.nH_2O + (2\text{-}n)\ H_2O$ à $H_4SiO_4$ (= $SiO_2 + 2\ H_2O$) | |
| 13 | X | Cation exchange | $Ca^{2+} + Na_aK_bMg_c\text{-}EXCH$ ßà $cMg^{2+} + aNa^+ + bK^+ + Ca\text{-}EXCH$ | # |
| 14 | - | Halite dissolution | $NaCl + H_2O$ à $Na^+ + Cl^- + H_2O$ | |
| 15 | - | Gypsum dissolution | $CaSO_4.2H_2O + H_2O$ à $Ca^{2+} + SO_4^{2-} + 3\ H_2O$ | |

$: X = 0 Y = 0 #: ½(a+b) + c = 1.0, c = ΔMg - x

Tritium at trace level was analyzed by the Institut für Umweltphysik (Abt. Ozeanographie, Universität Bremen, Germany) by analysis of daughter $^3He$ after 6 months of storage in the laboratory, using a sector field mass-spectrometer (MAP 215-50). The samples for $^{13}C$ and $^{14}C$ were stored in fully filled and perfectly closed glass bottles, sterilized by an $I_2$-KI solution, and kept in the dark at 0–5 °C. CIO analyzed $^{13}C$ by isotope-ratio mass spectrometry, and $^{14}C$ by 2.5 MV accelerator mass spectrometry. The $^{14}C$ results are reported as denormalized without correction for decay in the period 1950–2022, in accordance with Mook and Van der Plicht (1999). The approximate precision (reported by the laboratory) of the analyzed isotopes is indicated in Table 6.

### 2.5. Coastal North Sea water

It is important to discern the mixing of 2 watertypes in Coastal North Sea water (CNS) along the Dutch coast: (open) ocean water and river water from the Rhine, Meuse and Scheldt. The average fluvial fraction ($f_{R\text{-}CNS}$) is calculated by using Cl as a conservative tracer in a binary mixture:

$$f_{R-CNS} = (Cl_O - Cl_{CNS}) \ / \ (Cl_O - Cl_R) \quad (2)$$

$$\text{With}: Cl_R = 0.875\ Cl_{RR} + 0.08\ Cl_{MR} + 0.046\ Cl_{SR} \quad (3)$$

Where: Cl concentrations in mg/L; subscript CNS = Coastal North Sea; subscript R = discharge weighted mixture of the rivers Rhine ($Cl_{RR}$), Meuse ($Cl_{MR}$) and Scheldt ($Cl_{SR}$); and subscript O = Atlantic Ocean Water as a proxy of the North Sea far away from the coast (>70 km).

The average ocean fraction in CNS ($f_{O,CNS}$) equals 1 – $f_{R,CNS}$, and the concentration of parameter C in CNS is given by:

$$C_{CNS} = \left(1 - f_{R,CNS}\right) C_O + f_{R,CNS}\ C_R \quad (4)$$

The estimated high age of intruded CNS water justifies taking pre-industrial fluvial water qualities. With $Cl_O$ = 19,805 mg/L (White, 2013) and $Cl_{CNS}$ = 16,800 mg/L (Stuyfzand, 1993b) equations (2) and (3) yield $f_{R\text{-}CNS}$ = 0.1518, which is assumed constant on the study site.

With the established $f_{R\text{-}CNS}$ and the composition of both endmembers (ocean water and fluvial mixture; Table 3) the composition of CNS water before the start of heavy fluvial pollution was estimated using Eq. (4). Data in Molt (1961), Zuurdeeg (1980) and Stuyfzand (1991, 1993b) were used for the main and trace constituents. Stable isotope data of CNS water near Zandvoort were obtained from Mook (1970, 2005) or calculated from the established coastal mixing of Atlantic Ocean Water (AtOc) with the fluvial mixture. Harwood et al. (2008) mention an $^{18}O$ delta value of +0.4 ‰ for North Atlantic sub-polar mode water, which enters the North Sea between Scotland and Norway.

The deduced high age of infiltrated CNS water (observed $^3H$ = 0 TU) excludes complications due to contributions of thermonuclear bomb-pulses to the $^3H$ and $^{14}C$ levels. The $^{14}C$ activity of the North Sea and AtOc show a structural depletion relative to the coeval atmosphere. An average age set-back of 508 years (based on Heaton et al., 2020; Scourse et al., 2012) is accounted for by reducing the $^{14}C$ input from 100 to 94.04 pmC. The age set-back for the combined fluvial inputs is probably 2 ka (Lanting and Van Der Plicht, 1998), reducing its $^{14}C$ activity from 100 to 78.5 pmC. Its 15.18 % mixing with AtOc leads to $^{14}C$ = 0.1518*78.5+ (1–0.1518)*94.04 = 91.68 pmC in CNS water.

### 2.6. Admixed deep dune groundwater in intruded North Sea water

Both investigated flow paths of intruded North Sea water show some admixing of fresh, deep dune groundwater, due to vertical dispersion across the transition zone. This dispersion was enhanced by the upward movement of this interface during overexploitation (1902–1957) and subsequent downward movement when basin recharge of Rhine River water replaced the extraction of deep dune groundwater (as of 1957). The fraction of dune groundwater, river and ocean water in 'intruded' CNS (as sampled from wells) was calculated as follows. We assume that the chlorinity of CNS water did not change during the past 6 ka, and that the $f_R/f_O$ ratio in 'intruded' CNS remained constant as in CNS at 0.1518/(1–0.1518) = 0.179:

$$f_D = 1 - f_O - f_R \quad (5)$$

$$\text{with}: f_O = (Cl_M - Cl_D) \ / \ \left\{(Cl_{CNS} - Cl_D)\left(1 + f_{R,CNS} \ / \ f_{O,CNS}\right)\right\} \quad (6)$$

$$f_R = \left(f_{R,CNS} \ / \ f_{O,CNS}\right) f_O = 0.179\ f_O \quad (7)$$

Where: $Cl_M$ = measured Cl concentration of 'intruded' CNS [mg/L]; $Cl_D$ = Cl concentration of admixed, fresh dune groundwater [mg/L]; $f_D$, $f_O$, $f_R$ = dune, ocean and river water fraction in 'intruded' CNS [-].

**Table 4**
Inorganic composition of the sampled intruded coastal North Sea water along the northern and southern transect (Fig. 3), with 5 relevant input waters. These are: coastal North Sea water (CNS) near Zandvoort aan Zee, consisting of a mix of Atlantic Ocean water (AtOc) with a mix of Rhine, Meuse and Scheldt river water, and 2 types of deep dune groundwater admixed in the samples. The grey colored samples contain 35 % admixed deep dune groundwater (composition listed), the others are composed of nearly pure coastal North Sea water. Mean North and mean South without samples with Cl < 13,000 mg/L. Mean values in red if North and South differ by >20 %. X-HWL = distance to current High Water Line North Sea. $O_2$ and $NO_3$ in all CNS infiltrate samples <0.5 mg/L.

| Water type | Sampling | depth | X-HWL | EC | pH | Temp | Cl | SO4 | Alk | F | PO4 | Na | K | Ca | Mg | Fe | Mn | NH4 | SiO2 | DOC |
|---|---|---|---|---|---|---|---|---|---|---|---|---|---|---|---|---|---|---|---|---|
| or well | Year | m ASL | km | µS/cm | - | oC | mg/L | | | | | | | | | | | | | |
| *Precision [%]* | *0* | *0.5* | *0.5* | *1.6* | *1.3* | *8.8* | *1.8* | *2.2* | *4.7* | - | - | *1.9* | *3.7* | *6.4* | *3.0* | *5.5* | *10.7* | - | *30* | - |
| Deep dune 1# | 1977 | -77 | 3.6 | 580 | 7.30 | 10.7 | 36 | 0 | 389 | 0.03 | 1.82 | 51 | 10 | 61 | 20 | 2.2 | 0.2 | 2.8 | 32.0 | 5.2 |
| Deep dune 2# | 1978 | -104 | 7.2 | 1113.5 | 7.50 | 11.8 | 193 | 1 | 478 | 0.10 | 1.75 | 186 | 17.3 | 50.5 | 24.2 | 1.05 | 0.27 | 4.59 | 16.0 | 8.0 |
| Rhine +MS $ | 1880 | 10 | 65.0 | 310 | 7.50 | 10.0 | 13 | 35 | 160 | 0.11 | 0.10 | 6.0 | 4.9 | 50.6 | 10.0 | 0.05 | 0.05 | 0.05 | 10.0 | 2.0 |
| AtOc | 1991 | -1 | -700 | 47341 | 8.22 | 10.5 | 19805 | 2775 | 145 | 1.42 | 0.06 | 11020 | 408 | 422 | 1322 | 0.002 | 0.0002 | 0.03 | 4.4 | 0.7 |
| Coastal Nsea | 1880 | -1 | -0.8 | 39000 | 7.89 | 10.5 | 16800 | 2359 | 147 | 1.22 | 0.06 | 9348 | 347 | 366 | 1122 | 0.050 | 0.050 | 0.40 | 5.2 | 0.9 |
| Transect North 24H287 | 2019 § | -84 | 0.04 | 40350 | 7.04 | 10.1 | 16299 | 2234 | 185 | 0.47 | 2.81 | 9051 | 313 | 347 | 1095 | 9.9 | 0.8 | 7.1 | 9.9 | 3.5 |
| 24H597 | 2019 § | -100 | 0.76 | 41050 | 7.23 | 10.5 | 16646 | 2183 | 202 | 0.40 | 3.10 | 9245 | 320 | 363 | 1093 | 8.9 | 0.63 | 8.0 | 10.7 | 3.5 |
| 24H473 | 2019 § | -171 | 1.91 | 42000 | 7.23 | 10.9 | 16724 | 2158 | 240 | 0.44 | 2.73 | 9262 | 312 | 370 | 1112 | 10.0 | 0.65 | 3.4 | 11.9 | 3.5 |
| 24H507 | 2019 § | -133 | 2.00 | 42000 | 7.19 | 10.7 | 16826 | 2217 | 236 | 0.30 | 2.94 | 9361 | 312 | 375 | 1105 | 10.9 | 0.71 | 4.5 | 11.6 | 3.8 |
| 24H716 | 2019 § | -112 | 2.53 | 41000 | 7.23 | 11.0 | 16643 | 2197 | 316 | 0.16 | 2.54 | 9309 | 294 | 377 | 1083 | 11.1 | 0.69 | 5.5 | 11.7 | 5.4 |
| 24H330 | 2019 § | -120 | 4.26 | 41800 | 7.26 | 11.2 | 17043 | 2291 | 267 | 0.18 | 2.68 | 9474 | 326 | 348 | 1154 | 9.6 | 0.58 | 5.6 | 11.1 | 4.6 |
| 24H332 | 2019 § | -183 | 4.54 | 40550 | 7.29 | 10.4 | 15681 | 2084 | 272 | 0.02 | 1.51 | 8642 | 265 | 393 | 1064 | 12.0 | 0.80 | 7.3 | 16.3 | 3.4 |
| 25C8 | 2019 § | -134 | 4.88 | 40100 | 7.25 | 10.2 | 16471 | 2159 | 243 | 0.47 | 1.66 | 9149 | 285 | 394 | 1077 | 11.9 | 0.80 | 6.1 | 12.5 | 3.6 |
| 25C332 | 2019 § | -135 | 5.75 | 40350 | 7.24 | 10.6 | 15846 | 2160 | 262 | 0.30 | 1.51 | 8849 | 270 | 384 | 1036 | 12.9 | 0.81 | 5.3 | 11.7 | 4.0 |
| 25C12 | 2019 § | -165 | 8.61 | 38150 | 7.25 | 11.3 | 15178 | 2017 | 293 | 0.15 | 1.16 | 8370 | 244 | 439 | 1003 | 15.0 | 0.73 | 7.3 | 15.5 | 4.0 |
| 25C12 | 2019 § | -128 | 8.61 | 29050 | 7.29 | 11.1 | 11014 | 1587 | 401 | 0.13 | 0.79 | 6079 | 174 | 357 | 770 | 11.0 | 0.49 | 7.9 | 10.8 | 5.4 |
| 25C294 | 1987 | -60 | 9.60 | 24500 | 7.20 | 11.7 | 9234 | 748 | 1171 | 0.06 | 4.56 | 5150 | 110 | 430 | 590 | 12.3 | 0.17 | 21.3 | 17.6 | - |
| Transect South 24H1331 | 2019 § | -94 | 0.75 | 39450 | 7.26 | 11.1 | 16211 | 2156 | 212 | 0.20 | 0.81 | 9030 | 311 | 363 | 1056 | 6.7 | 0.8 | 8.2 | 10.9 | 3.3 |
| 24H1248 | 2019 § | -93 | 1.38 | 39850 | 7.23 | 10.6 | 15954 | 2108 | 227 | 0.18 | 1.89 | 8867 | 287 | 368 | 1045 | 9.2 | 0.84 | 16.1 | 12.0 | 4.1 |
| 24H1305 | 2019 § | -113 | 2.10 | 39950 | 7.20 | 11.5 | 15984 | 2142 | 223 | 0.14 | 1.60 | 8877 | 285 | 385 | 1050 | 11.4 | 0.85 | 7.8 | 11.6 | 3.9 |
| 24H1325 | 2019 § | -123 | 3.34 | 27850 | 7.18 | 10.7 | 10883 | 1373 | 388 | 0.10 | 0.71 | 5834 | 114 | 620 | 653 | 14.9 | 1.65 | 10.9 | 13.2 | 4.6 |
| 24H750 | 2019 § | -112 | 3.64 | 39200 | 7.07 | 11.3 | 15714 | 2043 | 253 | 0.22 | 2.28 | 8647 | 249 | 445 | 1026 | 28.3 | 1.66 | 11.4 | 15.3 | 7.1 |
| 24H718 | 2019 § | -114 | 4.05 | 38100 | 7.06 | 10.3 | 15219 | 2042 | 268 | 0.10 | 1.57 | 8385 | 229 | 444 | 1006 | 20.8 | 1.35 | 12.7 | 13.3 | 5.4 |
| 24H607 | 2019 § | -123 | 5.27 | 36250 | 7.04 | 11.2 | 14383 | 1982 | 316 | 0.09 | 1.87 | 7683 | 127 | 783 | 916 | 14.4 | 1.70 | 6.3 | 13.0 | 5.1 |
| 24H600 | 1987 | -125 | 8.00 | 26000 | 7.00 | 12.2 | 9901 | 1440 | 383 | - | 1.35 | 5300 | 79 | 680 | 585 | 12.7 | 2.18 | 12.3 | 12.8 | 5.7 |
| Mean North | 2019 § | -133 | 3.53 | 40735 | 7.22 | 10.7 | 16336 | 2170 | 252 | 0.29 | 2.26 | 9071 | 294 | 379 | 1082 | 11.2 | 0.7 | 6.0 | 12.3 | 3.9 |
| Mean South | 2019 § | -108 | 2.86 | 38800 | 7.14 | 11.0 | 15578 | 2079 | 250 | 0.15 | 1.67 | 8582 | 248 | 465 | 1016 | 15.1 | 1.2 | 10.4 | 12.7 | 4.8 |

1# = well 24H389-77; #2 = mean wells 25C332-111 + 25C12-97 $: Mixture of 87.4% Rhine + 8% Meuse (M) + 4.6% Scheldt (S)

In the following, we discern CNS infiltration water (prior to infiltration, with $f_D = 0$), pure CNS infiltrate (infiltrated CNS with $f_D = 0$), and CNS infiltrate (infiltrated CNS with $f_D > 0$).

### 2.7. Quantification of quality changes in aquifer

The concentration change of any compound C (ΔC) in 'intruded' CNS, corrected for the admixing of dune groundwater, is calculated by subtracting the input ($C_{CNS}$) from the corrected measured concentration ($C_{M,COR}$) as follows:

$$\Delta C = C_{M,COR} - C_{CNS} \quad (8)$$

$$C_{CNS} = f_{O,CNS}\, C_O + f_{R,CNS}\, C_R = \left(f_O\, C_O + f_R\, C_R\right) \Big/ \left(f_O + f_R\right) \quad (9)$$

$$C_{M,COR} = \left\{C_M - \left(1 - f_O - f_R\right) C_D\right\} \Big/ \left(f_O + f_R\right) \quad (10)$$

The term ΔC can subsequently be attributed to various reactions via mass balancing.

### 2.8. Quantification of reactions by mass balancing

The dominant hydrogeochemical reactions between an arbitrary starting and ending point in a flow system can be identified and quantified by drawing up a mass balance (Plummer and Glynn, 2013; Domenico and Schwartz, 1998). The chemical mass balance (CMB) is based on the sum of input ($C_{CNS}$) and a selection of linear reaction equations (here 15), that best match the output ($C_{M,COR}$), thus for each solute:

$$C_{M,COR} = C_{CNS} + \sum_{R=1}^{R=15} \Delta C_R \quad (11)$$

Where: C = solute concentration [mmol/L]; $\Delta C_R$ = concentration change of C by reaction R [mmol/L], which can be 0 for some reactions; $C_{M,COR}$ = solute concentration in sampled CNS infiltrate corrected for admixed dune groundwater [mmol/L].

The basic assumption is that the chemistry of the output is genetically linked to the input. This does not necessitate both samples to be taken exactly from the same flow path, but they need to be representative of the respective hydrosome from which the sample was taken. Neither is there any need for the system to be in steady state.

The Excel spreadsheet code Reactions+ (R+; Stuyfzand and Stuurman, 2008; Stuyfzand, 2011) was modified to specifically address Salt Water Intrusion: R + SWI. The changes include among others: addition of $^{13}C$ and $^{14}C$ (with age dating), and utilization of Excel's Solver routine as optimization method, which includes the option to slightly adjust the input of a few main constituents within bounds dictated by analytical uncertainties. The entire CMB involves 18 solutes, the isotopes $^{13}C$ and

**Table 5**
Trace element composition of the sampled intruded coastal North Sea water along the northern and southern transect (Fig. 3), with 5 relevant input waters. Further explanations in heading of Table 3.

| Water type | | depth | X-HWL | As | B | Ba | Br | Co | Cr | Cu | Li | Mo | Ni | Pb | Rb | Sb | Se | Sr | U | V | Zn |
|---|---|---|---|---|---|---|---|---|---|---|---|---|---|---|---|---|---|---|---|---|---|
| or well | | m ASL | km | µg/L | | | | | | | | | | | | | | | | | |
| *Precision [%]* | | *0.5* | *0.5* | *-* | *14* | *30* | *-* | *-* | *-* | *-* | *-* | *31* | *-* | *-* | *5* | *-* | *-* | *3* | *-* | *21* | *-* |
| Deep dune 1# | | -77 | 3.6 | 1.0 | 136 | 30 | 140 | 0.3 | 0.29 | 1.5 | 6 | 0.1 | 0.1 | 0.1 | 3.00 | 0.03 | 0.01 | 400 | 0.02 | 0.40 | 5 |
| Deep dune 2# | | -104 | 7.2 | 1.0 | 332 | 139 | 666 | 0.32 | 0.27 | 0.76 | 10 | 0.07 | 0.2 | 0.1 | 1.84 | 0.02 | 0.04 | 317 | 0.001 | 0.42 | 16 |
| Rhine +MS | | 10 | 65.0 | 0.5 | 15 | 30 | 42 | 0.14 | 0.5 | 0.7 | 5 | 0.9 | 1.2 | 0.1 | 4 | 0.07 | 0.25 | 510 | 0.7 | 1 | 14 |
| AtOc | | -1 | -700 | 1.23 | 4610 | 15 | 69000 | 0.002 | 0.20 | 0.15 | 185 | 11.0 | 0.49 | 0.03 | 124 | 0.24 | 0.16 | 7930 | 3.3 | 1.8 | 0.4 |
| Coastal Nsea | | -1 | -0.8 | 2.5 | 3912 | 17 | 58532 | 0.20 | 0.2 | 0.2 | 158 | 9.5 | 0.6 | 0.04 | 106 | 0.21 | 0.17 | 6790 | 2.9 | 1.7 | 2.4 |
| Transect North | 24H287 | -84 | 0.04 | 0.7 | 2623 | 90 | 58635 | 0.27 | 0.51 | 915 | 94 | 4.4 | 1.2 | 73.2 | 46 | 1.2 | 0.08 | 6901 | 0.01 | 0.9 | 521 |
| | 24H597 | -100 | 0.76 | 2.2 | 2715 | 87 | 58172 | 0.48 | 0.54 | 0.58 | 88 | 4.5 | 0.3 | 0.40 | 51 | 0.3 | 0.09 | 6908 | 0.01 | 0.9 | 20 |
| | 24H473 | -171 | 1.91 | 0.6 | 2749 | 99 | 60058 | 0.14 | 0.51 | 0.04 | 89 | 4.3 | 0.3 | 0.05 | 57 | 0.6 | 0.10 | 7200 | 0.02 | 0.7 | 12 |
| | 24H507 | -133 | 2.00 | 3.4 | 2790 | 77 | 60066 | 0.72 | 0.58 | 0.00 | 89 | 3.9 | 0.7 | 0.26 | 51 | 0.5 | 0.18 | 6994 | 0.02 | 1.0 | 21 |
| | 24H716 | -112 | 2.53 | 7.3 | 2653 | 180 | 57509 | 3.59 | 0.56 | 0.06 | 102 | 1.8 | 1.9 | 0.02 | 40 | 0.3 | 0.20 | 6917 | 0.03 | 1.1 | 1021 |
| | 24H330 | -120 | 4.26 | 1.7 | 2745 | 178 | 57681 | 0.16 | 0.60 | 0.03 | 81 | 3.7 | 0.1 | 0.10 | 53 | 0.9 | 0.18 | 6901 | 0.02 | 1.1 | 13 |
| | 24H332 | -183 | 4.54 | 0.2 | 2089 | 107 | 55581 | 0.08 | 0.26 | 0.47 | 99 | 1.6 | 0.1 | 0.16 | 25 | 1.4 | 0.08 | 7005 | 0.02 | 0.4 | 10 |
| | 25C8 | -134 | 4.88 | 0.1 | 2286 | 113 | 59099 | 0.05 | 0.23 | 11.5 | 107 | 2.3 | 0.1 | 35.0 | 29 | 0.6 | 0.05 | 7196 | 0.01 | 0.5 | 247 |
| | 25C332 | -135 | 5.75 | 0.2 | 2061 | 101 | 57524 | 0.06 | 0.25 | 0.10 | 99 | 2.0 | 0.1 | 0.03 | 31 | 0.7 | 0.08 | 7067 | 0.03 | 0.6 | 11 |
| | 25C12 | -165 | 8.61 | 0.9 | 1989 | 158 | 53654 | 0.07 | 0.19 | 0.10 | 104 | 0.6 | 0.2 | 0.01 | 27 | 0.1 | 0.21 | 6495 | 0.03 | 0.5 | 9 |
| | 25C12 | -128 | 8.61 | 0.4 | 1949 | 140 | 39073 | 0.07 | 0.26 | 0.10 | 74 | 1.1 | 0.2 | 0.05 | 18 | 0.0 | 0.14 | 5030 | 0.09 | 0.5 | 21 |
| Transect South | 24H1331 | -94 | 0.75 | 2.2 | 2534 | 98 | 57270 | 2.71 | 0.61 | 0.21 | 124 | 5.1 | 1.2 | 0.00 | 51 | 0.2 | 0.12 | 6756 | 0.07 | 2.4 | 15 |
| | 24H1248 | -93 | 1.38 | 1.3 | 2291 | 148 | 54468 | 0.15 | 0.39 | 0.10 | 79 | 2.9 | 0.4 | 0.02 | 50 | 0.8 | 0.04 | 7225 | 0.05 | 0.8 | 14 |
| | 24H1305 | -113 | 2.10 | 0.2 | 2488 | 170 | 55706 | 0.09 | 0.39 | 0.04 | 89 | 2.5 | 0.1 | 0.10 | 39 | 1.0 | 0.14 | 6822 | 0.02 | 0.8 | 8 |
| | 24H1325 | -123 | 3.34 | 0.1 | 534 | 197 | 36795 | 0.93 | 0.33 | 0.10 | 69 | 1.0 | 0.3 | 0.10 | 13 | 0.4 | 0.03 | 5618 | 0.04 | 0.4 | 18 |
| | 24H750 | -112 | 3.64 | 1.7 | 1226 | 150 | 55778 | 0.46 | 0.72 | 0.18 | 53 | 1.2 | 0.3 | 0.16 | 33 | 1.1 | 0.13 | 6606 | 0.01 | 1.3 | 19 |
| | 24H718 | -114 | 4.05 | 0.7 | 1153 | 152 | 52410 | 0.17 | 0.38 | 0.02 | 73 | 0.8 | 0.2 | 0.17 | 28 | 1.1 | 0.08 | 6707 | 0.01 | 0.7 | 13 |
| | 24H607 | -123 | 5.27 | 1.2 | 557 | 232 | 48984 | 0.32 | 3.00 | 0.13 | 76 | 1.5 | 0.3 | 0.15 | 25 | 0.1 | 0.19 | 6100 | 0.00 | 0.7 | 19 |
| Mean North | | -133 | 3.53 | 1.7 | 2522 | 133 | 57798 | 0.56 | 0.47 | 0.16 | 95.3 | 2.8 | 0.50 | 0.12 | 40.7 | 0.66 | 0.12 | 6939 | 0.02 | 0.76 | 14.5 |
| Mean South | | -108 | 2.86 | 1.2 | 1611 | 175 | 54103 | 0.65 | 0.54 | 0.11 | 82.2 | 2.5 | 0.42 | 0.10 | 38.1 | 0.73 | 0.12 | 6611 | 0.03 | 1.18 | 14.9 |

**Table 6**
Isotopic composition and calculated parameters of the sampled intruded coastal North Sea water along the northern and southern transect (Fig. 3), with 5 relevant input waters. Further explanation in heading of Table 4. 'Mean North' without 25C12-128, 'Mean South' without 24H1325-123. Mean values in red if differing by >20 %. Distance HWL (High Water Line North Sea) = current position for all wells; $^{3}H$ and $^{14}C$ data for the 3 surface waters refer to a Late Holocene period before 1953. $^{14}C_{DIC}$ uncorrected for decay in period 2022-1950.

| Water type | | depth | X-HWL | $f_O$ | $f_D$ | $f_R$ | BEX | DIC | Mineral Saturation Index ($SI_M$) | | | | | | | | $^{2}H$ | $^{18}O$ | $^{3}H$ | $\delta^{13}C_{DIC}$ | $^{14}C_{DIC}$ |
|---|---|---|---|---|---|---|---|---|---|---|---|---|---|---|---|---|---|---|---|---|---|
| or well | | m ASL | km | fraction in sample | | | meq/L | mmol/L | calc | dol | sid | rhod | gyps | barite | fluo | halite | ‰ SMOW | | TU | ‰ VPDB | pmC |
| *Precision [unit]* | | *0.5* | *0.02* | *0.01* | *0.01* | *0.01* | *0.10* | *0.10* | *0.30* | | | | | | | | *1* | *0.1* | *0.03* | *0.1* | *0.2* |
| Deep dune 1# | | -77.0 | 3.63 | 0.00 | 1.00 | 0.00 | 3.02 | 7.20 | 0.00 | -0.46 | 0.33 | -0.81 | <-10 | <-10 | -3.65 | -7.4 | -42.1 | -6.5 | 0 | -7.00 | 78.0 |
| Deep dune 2# | | -104.0 | 7.18 | 0.00 | 1.00 | 0.00 | 4.68 | 8.41 | 0.16 | 0.06 | 0.25 | -0.38 | -3.79 | -1.27 | -2.68 | -6.1 | -40.5 | -6.25 | 0 | -9.46 | 66.3 |
| Rhine +MS | | 10.0 | 65.00 | 0.00 | 0.00 | 1.00 | 0.82 | 2.84 | -0.25 | -1.16 | -11.01 | -1.53 | -2.10 | -0.23 | -2.43 | -8.7 | -68.7 | -9.31 | 4 | -10.6 | 78.52 |
| AtOc | | -1.0 | -2.00 | 1.00 | 0.00 | 0.00 | 0.00 | 2.34 | 0.57 | 1.79 | -11.01 | -4.11 | -0.53 | -0.14 | -1.56 | -2.6 | 2 | 0.4 | 0.6 | 1.00 | 94.04 |
| Coastal Nsea | | -1.0 | -0.80 | 0.85 | 0.00 | 0.15 | 0.07 | 2.46 | 0.26 | 1.14 | -11.01 | -1.95 | -0.59 | -0.09 | -1.56 | -2.7 | -10.3 | -1.3 | 1.12 | -0.76 | 91.68 |
| Transect North | 24H287 | -83.7 | 0.04 | 0.82 | 0.03 | 0.15 | -0.79 | 3.44 | -0.49 | -0.33 | -0.49 | -1.51 | -0.62 | 0.62 | -2.38 | -2.8 | -9.2 | -1.3 | <0.03 | -7.89 | 70.58 |
| | 24H597 | -99.7 | 0.76 | 0.84 | 0.01 | 0.15 | -2.85 | 3.56 | -0.24 | 0.15 | -0.30 | -1.36 | -0.62 | 0.61 | -2.45 | -2.8 | -9 | -1.51 | 0.07 | -6.25 | 71.93 |
| | 24H473 | -170.7 | 1.91 | 0.84 | 0.00 | 0.16 | -3.12 | 4.24 | -0.15 | 0.33 | -0.17 | -1.27 | -0.62 | 0.65 | -2.39 | -2.8 | -7.4 | -1.27 | <0.03 | -9.34 | 61.96 |
| | 24H507 | -132.5 | 2.00 | 0.85 | 0.00 | 0.15 | -2.48 | 4.20 | -0.19 | 0.24 | -0.19 | -1.28 | -0.61 | 0.54 | -2.69 | -2.7 | -5.2 | -1.01 | <0.03 | -10.0 | 64.93 |
| | 24H716 | -111.9 | 2.53 | 0.84 | 0.01 | 0.15 | -1.45 | 5.60 | -0.03 | 0.56 | -0.01 | -1.12 | -0.60 | 0.91 | -3.21 | -2.8 | -7 | -1.37 | <0.03 | -9.2 | 45.96 |
| | 24H330 | -119.7 | 4.26 | 0.86 | 0.00 | 0.14 | 0.27 | 4.68 | -0.11 | 0.46 | -0.12 | -1.25 | -0.64 | 0.90 | -3.27 | -2.7 | -7 | -1.14 | <0.03 | -7.58 | 66.86 |
| | 24H332 | -183.0 | 4.54 | 0.79 | 0.00 | 0.21 | -3.64 | 4.80 | 0.00 | 0.58 | 0.04 | -1.05 | -0.59 | 0.69 | -4.96 | -2.8 | -11.4 | -1.88 | <0.03 | -11.17 | 42.79 |
| | 25C8 | -133.6 | 4.88 | 0.83 | 0.02 | 0.15 | -3.93 | 4.31 | -0.10 | 0.37 | -0.07 | -1.15 | -0.58 | 0.74 | -2.28 | -2.8 | -7.5 | -1.46 | <0.03 | -9.4 | 41.59 |
| | 25C332 | -134.8 | 5.75 | 0.80 | 0.06 | 0.14 | -1.85 | 4.66 | -0.08 | 0.41 | 0.00 | -1.12 | -0.58 | 0.69 | -2.63 | -2.8 | -9.2 | -1.39 | 0.07 | -8.75 | 36.29 |
| | 25C12 | -164.6 | 8.61 | 0.77 | 0.10 | 0.14 | -5.89 | 5.20 | 0.06 | 0.63 | 0.16 | -1.07 | -0.54 | 0.86 | -3.12 | -2.8 | -15.1 | -1.89 | 0.10 | -5.69 | 49.27 |
| | 25C12 | -127.6 | 8.61 | 0.55 | 0.35 | 0.10 | -0.63 | 7.12 | 0.19 | 0.85 | 0.30 | -1.00 | -0.65 | 0.83 | -2.99 | -3.1 | -21.4 | -3.11 | 0.09 | -7.71 | 49.73 |
| Transect South | 24H1331 | -94.4 | 0.75 | 0.82 | 0.04 | 0.15 | -2.35 | 3.75 | -0.18 | 0.25 | -0.35 | -1.21 | -0.61 | 0.66 | -3.02 | -2.8 | -10.1 | -1.5 | <0.03 | -6.14 | 50.10 |
| | 24H1248 | -93.0 | 1.38 | 0.81 | 0.05 | 0.14 | -3.17 | 4.03 | -0.18 | 0.24 | -0.23 | -1.18 | -0.61 | 0.85 | -3.11 | -2.8 | -9.7 | -1.33 | <0.03 | -9.67 | 45.23 |
| | 24H1305 | -113.0 | 2.10 | 0.81 | 0.05 | 0.14 | -3.25 | 4.00 | -0.19 | 0.20 | -0.16 | -1.20 | -0.59 | 0.90 | -3.33 | -2.8 | -8.6 | -1.29 | 0.06 | -6.02 | 51.38 |
| | 24H1325 | -123.1 | 3.34 | 0.55 | 0.35 | 0.10 | -18.50 | 7.10 | 0.32 | 0.78 | 0.33 | -0.58 | -0.45 | 1.00 | -2.76 | -3.1 | -21.5 | -2.95 | <0.03 | -12.57 | 40.09 |
| | 24H750 | -112.0 | 3.64 | 0.79 | 0.06 | 0.14 | -8.02 | 4.65 | -0.18 | 0.17 | 0.18 | -0.97 | -0.54 | 0.82 | -2.78 | -2.8 | -11.7 | -1.82 | 0.11 | -9.67 | 49.59 |
| | 24H718 | -114.4 | 4.05 | 0.77 | 0.09 | 0.14 | -6.56 | 4.99 | -0.17 | 0.16 | 0.07 | -1.04 | -0.53 | 0.85 | -3.50 | -2.8 | -12.6 | -1.9 | 0.10 | -10.14 | 48.47 |
| | 24H607 | -122.8 | 5.27 | 0.73 | 0.14 | 0.13 | -21.87 | 5.94 | 0.17 | 0.56 | 0.01 | -0.84 | -0.29 | 1.04 | -3.15 | -2.9 | -14.16 | -2.53 | <0.03 | -11.78 | 54.31 |
| Mean North | | -133.4 | 3.53 | 0.82 | 0.02 | 0.15 | -2.57 | 4.47 | -0.13 | 0.34 | -0.11 | -1.22 | -0.60 | 0.72 | -2.94 | -2.8 | -8.8 | -1.42 | 0.03 | -8.527 | 55.22 |
| Mean South | | -108.2 | 2.86 | 0.79 | 0.07 | 0.14 | -7.54 | 4.56 | -0.12 | 0.26 | -0.08 | -1.07 | -0.53 | 0.86 | -3.15 | -2.8 | -11.1 | -1.73 | 0.05 | -8.90 | 49.85 |

$^{14}C$, the 15 reactions listed in Table 3, and the composition of reactive solid phases. Sedimentary organic matter (SOM), and carbonate minerals deserve special attention, because their composition may vary in both carbon isotopes and 'non-isotopic' elements such as N and P in SOM (see Table A1) and Ca, Mg and Fe in carbonates. Two interconnected parts of R + SWI are shown in Fig. A1 (CMB of main constituents) and Fig. A2 (CMB of both carbon isotopes), respectively.

After a first approximative solution of the 20 (including the carbon isotopes) by 15 matrix, Solver is applied to reach its predefined objective by varying selected cells within their set constraints. Details of Excel code R + SWI are given in Appendix A2.

An example of the CMB for $\delta^{13}C_{DIC}$, based on Reactions 1–11 in Tables 3 and is presented in Fig. A2. It is calculated as follows:

$$\delta^{13}C_{DIC,OUT} = \frac{\delta^{13}C_{CNS}DIC_{CNS} + A\ \Delta CO2_{\Sigma} + B\ \Delta HCO3_{\Sigma}}{DIC_{\Sigma}} \quad (12)$$

With :

$$A = \frac{\sum_{R=1}^{R=11}\left(\Delta^{13}C_{CO2,R+}\Delta CO2_{R+}\right) - \epsilon_{b/a}D}{\Sigma\Delta CO2_{R+} - D}$$

$$B = \frac{\sum_{R=1}^{R=11}\left(\Delta^{13}C_{HCO3,R+}\Delta HCO3_{R+}\right) + \epsilon_{b/a}D}{\Sigma\Delta HCO3_{R+} + D}$$

$$D = \sum_{R=1}^{R=11}(a \rightarrow b) - \sum_{R=1}^{R=10}(b \rightarrow a)$$

Where: A = weighted mean of $\delta^{13}C_{CO2}$ from all reactions producing $CO_2$ [‰ VPDB]; B = weighted mean of $\delta^{13}C_{HCO3}$ from all reactions producing $HCO_3$ [‰ VPDB]; D = net conversion of a (acid = $CO_2$) to b (bicarbonate = $HCO_3$), corrected for the reverse conversion [mmol/L]; $\varepsilon_{b/a} = 9866/T - 24.12$ = fractionation factor during equilibrium exchange with 'a' (= dissolved $CO_2$) converted to 'b' (=$HCO_3$), according to Mook and van der Plicht (1999) with T = temperature [K]; $\Delta CO2_{\Sigma}$, $\Delta HCO3_{\Sigma}$ = total net concentration change of $CO_2$ and $HCO_3$, respectively, by all reactions together [mmol/L]; $\Delta CO2_{R+}$, $\Delta HCO3_{R+}$ = concentration change of $CO_2$ and $HCO_3$, respectively, by 'producing' reaction R only, excluding fractionation effects (no gains by conversion of b to a or a to b) [mmol/L]; $\Sigma\Delta CO2_{R+}$, $\Sigma\Delta HCO3_{R+}$ = sum of all $\Delta CO2_{R+}$, $\Delta HCO3_{R+}$, respectively [mmol/L]; $\Delta^{13}C_{CO2,R+}$, $\Delta^{13}C_{HCO3,R+}$ = change of $\delta^{13}C_{CO2}$ and $\delta^{13}C_{HCO3}$, respectively, by 'producing' reaction R only, fractionation effects excluded [‰ VPDB]; $DIC_{\Sigma} = DIC_{CNS} + \Delta CO2_{\Sigma} + \Delta HCO3_{\Sigma}$ [mmol/L].

We did not further optimize each mass balance by changing the values of X in $Ca_{1-X}Mg_XCO_3$, Y in $Fe_{1-Y}Mn_YCO_3$, the $PO_4$ content of Fe $(OH)_3$ and SOM, and the $NH_4$ content of SOM.

For the DIC species, effects of isotopic fractionation during equilibrium shifts between dissolved $CO_2$ and $HCO_3$ (Mook, 2005; Clark and Fritz, 1997) are included. The temperature dependency of the $CO_2$ – $HCO_3$ fractionation factor is taken from Mook (2005). It is assumed that the temperature of infiltrating CNS remained constant at 10.5 °C during the entire Late Holocene period. Various complications in the isotopic mass balance are neglected, such as: recrystallization of carbonate solids, dissolution of primary silicate minerals, dissolution of $CaCO_3$ by humic acids, and exchange with or diffusion into/from semipervious layers. Also, the relatively small $^{13}C$ fractionation of $HCO_3$ - $CO_3$ – $CaCO_3$ is neglected.

### 2.9. Radiocarbon age dating

The $^{14}C$-age of infiltrated CNS ($t_{14C}$; year) was calculated as follows, applying 4 methods of increasing complexity (A-D) to determine parameter $^{14}C_{ND}$.

$$\text{For each sample}: t_{14C} = 8270 \ln\left(\frac{^{14}C_{ND}}{\xi\ ^{14}C_{M,COR}}\right) \quad (13)$$

Where: $^{14}C_{ND}$ = calculated $^{14}C$ activity of DIC in each groundwater sample, without decay, without admixing of dune groundwater, but with the diluting effect of carbonate mineral dissolution and SOM oxidation [pmC]; ξ = correction factor for the time elapsed between analysis and the year 1950, which is the standard lab reference. Here, ξ = 0.991 = EXP (-(2022-1950)/8267); $^{14}C_{M,COR}$ = measured $^{14}C$ corrected for admixed deep dune groundwater with approximately known $^{14}C$ [pmC].

Method A yields the conventional $^{14}C$ age by setting $^{14}C_{ND} = 100$ pmC, as usual (ignoring the diluting effect of reactions with the porous medium). Method B uses a fixed $^{14}C_{ND}$ value of 91.68 pmC (section 2.5), which is the calculated concentration of CNS infiltration water. This is more realistic than method A, but still lacking the diluting effects. Method C uses dissolved inorganic carbon (DIC) as indicator of $^{14}C$ dilution in a simplified way, and assumes a double layered reactive sediment composed of Holocene and Pleistocene deposits, each with a specific $^{14}C$ activity (Eq. (14)):

$$^{14}C_{ND} = \frac{^{14}C_0DIC_0 + \Delta DIC_{HOL}\left(^{14}C_0 + {}^{14}C_{S,HOL}\right)/2 + Q}{DIC_{M!}} \quad (14)$$

With:

$$DIC_{M!} = (DIC_M - (1 - f_D)DIC_D)/(1 - f_D)$$

$$Q = (DIC_{M!} - DIC_0 - \Delta DIC_{HOL})\left(^{14}C_0 + {}^{14}C_{S,PLEIST}\right)/2$$

Where: $DIC_0$ = in coastal North Sea before infiltration [mmol/L]; $DIC_M$ = as measured in intruded North Sea water samples = $(1\text{-}f_D)DIC_0 + f_D DIC_D + \Delta DIC_{HOL} + \Delta DIC_{PLEIST}$ [mmol/L]; $DIC_{M!} = DIC_M$ corrected for contribution of $DIC_D$ in deep (fresh) dune groundwater [mmol/L]; $\Delta DIC_{HOL}$, $\Delta DIC_{PLEIST}$ = DIC increase after passage of Holocene and Pleistocene sediments, respectively [mmol/L]; $^{14}C_0 = {}^{14}C$ of CNS before infiltration [pmC]; $^{14}C_{S,HOL}$, $^{14}C_{S,PLEIST} = {}^{14}C$ of solid carbon phases ($CaCO_3$ and SOM) within Holocene and Pleistocene deposits, respectively [pmC].

$DIC_0$ is assumed to equal the current coastal North Sea level of 2.46 mmol/L. $DIC_D$ was set at 7.20 mmol/L for samples with code 24H and at 8.41 for samples below aquitards B + C (Fig. 3; code 25C); $\Delta DIC_{HOL}$ was set at 0.6 mmol/L based on the observed DIC increase during passage of marine, calcareous Holocene deposits from 0.9 to 13 m BSL in nearby monitoring wells. $A^{14}C_0$ activity of 91.68 pmC was chosen as explained in section 2.5. $^{14}C_{S,HOL}$ was fixed at 60 pmC, corresponding with an average age of 4.225 ka for the calcareous Holocene deposits (Van der Valk, 1992), and $^{14}C_{S,PLEIST}$ at 0 pmC, as the calcareous Pleistocene layers are >55 ka old.

Method D also uses DIC as an indicator of $^{14}C$ dilution, but in a more sophisticated manner by summation of the 11 hydrogeochemical reactions in the carbon isotopic extension of the CMB of the main constituents (Fig. A2 of Appendix):

$$^{14}C_{ND} = \frac{^{14}C_0DIC_0 + \sum_{R=1}^{R=11}\left(^{14}C_R\Delta DIC_R\right) + 0.23\epsilon_{b/a}D}{D + DIC_{\Sigma}} \quad (15)$$

Where: $\Delta DIC_R$ = DIC concentration change by reaction R, see Fig. A2 in Appendic A for each of the 11 reactions [mmol/L]; $DIC_{\Sigma} = DIC_0 + \Sigma\Delta DIC_R$, which ideally equals DIC measured in intruded CNS after correction for dune water admixing using Eq. (10) [mmol/L]; $^{14}C_R = {}^{14}C$ of the ΔDIC assigned to reaction R [pmC]; D = as in Eq. (12).

Method D assumes a triple layered reactive sediment composed of relatively young seafloor sand, Holocene and Pleistocene deposits, each with a specific $^{14}C$ activity.

Methods A-D assume a simple flowtube approach with piston flow and without $^{14}C$ losses or gains by diffusion into/from semipervious layers or low permeability zones. The assumed fixed $^{14}C$ levels of CNS infiltration water and several Holocene sediments impact on the calculated $^{14}C$ age. Therefore a sensitivity analysis was initiated looking for

effects of varying the chosen values on the $^{14}C$ model D age (section 3.6, Table A2 and Fig. A3).

### 2.10. Direct age simulation

The variable density groundwater modeling software SEAWAT (Langevin & Guo 2006) was used to model the hydrological evolution along our northern transect since 3.5 ka BP. The specific goal was to simulate groundwater age using the 'direct age' approach by Goode (1996) and compare the pattern to the $^{14}C$-age inferred from the field data. To this aim the cross-sectional model by Nienhuis et al. (2014, 2017) was adapted by extending the western model boundary further offshore and by placing the start time at 3.5 ka BP. This starting point was chosen because no major shifts of the coastline have occurred since then. The initial concentration varied linearly from less than 4 g/L of chloride at the land surface to 17 g/L at 200 m below mean level, mimicking the salinity distribution caused by previous intrusion events (Delsman et al., 2014). Below the North Sea, groundwater chloride concentrations were assumed to be constant and equal to 17 g/L. Sea level was lower by 1.8 m at 3.5 ka BP and its rise since then was considered, as was the build-up of the coastal dune belt since 1000 AD. The reclamation of Lake Haarlemmermeer in 1852 and groundwater extraction since 1853 as well as artificial recharge since 1957 were included as described in Nienhuis et al. (2014). The direct age approach treats the age as a solute species that accumulates at a rate of 1. It was included as a second species in the SEAWAT model (salinity being the first) and in addition to accumulation it is subject to advection and hydrodynamic dispersion.

## 3. Results and discussion

### 3.1. Main constituents

The spatial distribution of the Cl concentration measured along both transects is shown in Fig. 3, together with the evolution of the fresh/salt interface (8415 mg/L = ½{16,800 + 30}).

Chloride was used as the principal indicator of the contribution of AtOc ($f_O$), river water ($f_R$) and dune water ($f_D$) to the composition of the sampled CNS infiltrate. The results obtained with fixed $f_O/f_R$ ratio using Eq. (4) are shown in Table 6.

The CNS intrusion front is situated at ca. 9 and 7 km from the coast along the northern and southern transect, respectively. There, the steeply declining concentrations of Cl, Na, K, Mg and $SO_4$ (Fig. 4, Table 4) mark the transition to brackish Holocene transgression water (hydrosome L in Fig. 2). This relict water is slowly bleeding out by exfiltration in the Haarlemmermeer polder. Negligible Cl changes over time in the deepest, saline parts (>120 m BSL) testify that the advancing CNS front already passed the most inland monitoring well 25C.12, 120 years ago (see A4).

The concentrations of Cl, Na, Ca and Mg as well as EC hardly change compared to CNS along the first four km of the northern, and two km of the southern transect. However, the other dissolved components have already substantially changed in the first wells (24H287 and 24H1331) where $HCO_3$, DIC, $PO_4$, Fe, Mn, $NH_4$, $SiO_2$ and DOC have increased,

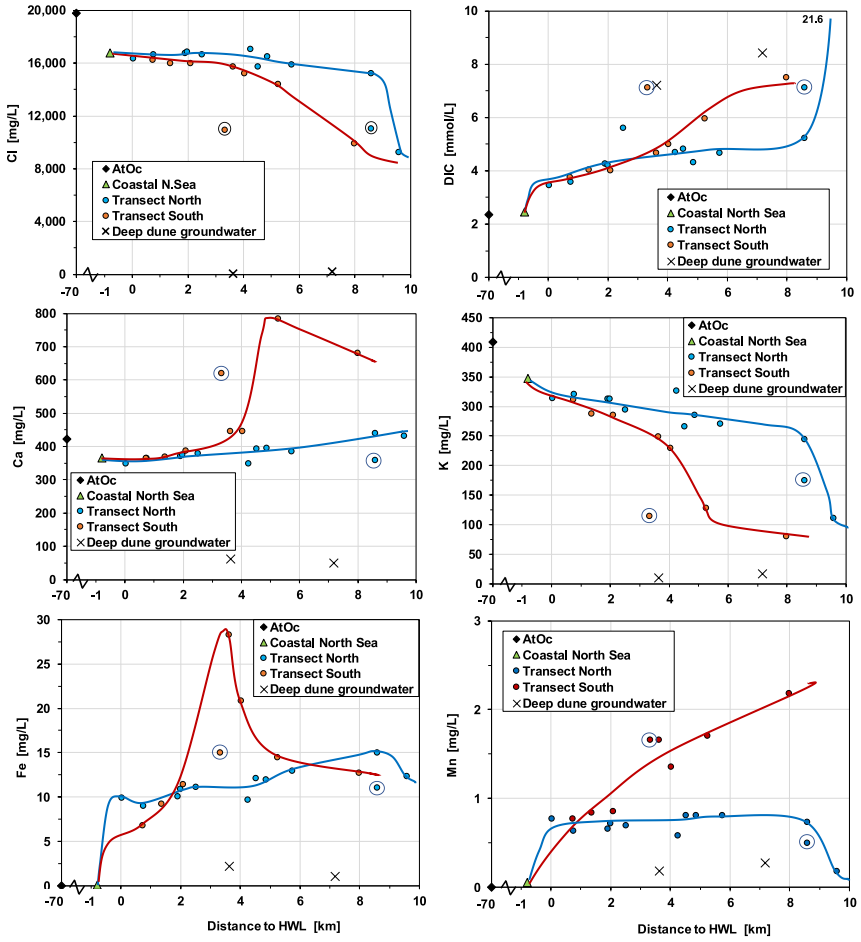


**Fig. 4.** Changes of main constituents of infiltrated North Sea water down the flow path, at 90–170 m BSL in the semiconfined sand aquifer, moving towards the Haarlemmermeer polder. Based on data in Table 3. *The 2 encircled data points indicate substantial admixing of fresh dune groundwater (ca. 35 %). HWL = High Water Line North Sea.*

while pH, K and $SO_4$, have decreased. Moreover, all $O_2$ and $NO_3$ has been consumed. These changes mainly occur in aquitards A and C below the seafloor because (sub)horizontal flow through sandy aquifers 3(A)-5 does not lead to substantial changes up to the mentioned 4 and 2 km travel distance.

Further downgradient of those distances, up to the CNS intrusion front, changes occur due to increased admixing of dune groundwater. Excluding two samples that have extreme $f_D$ values of 35 %, $f_D$ rises from 0 to ca. 14 % (see Table 6), and cation exchange because of salinization (salt water expelling brackish groundwater). The increased dune groundwater component is due to widening of the fresh-salt transition zone, downgradient of the deep groundwater divide (See Fig. A6).

Cation exchange is more pronounced along the southern transect, where the Ca peak is due to a more pronounced cation exchange for K (see Fig. 4), Na and Mg. In the southern transect, the more pronounced DIC increase is due to the admixing of the expelled brackish groundwater as evidenced by the Cl decline (Fig. 4). This decline is not due to dune groundwater admixing but due to the mixing with Relic, Holocene, lagoonal groundwater (Fig. 2).

In an aquifer system practically without dolomite, cation exchange during saltwater intrusion (SWI) or freshwater intrusion (FWI) can be quantified with the Base Exchange index BEX (Stuyfzand, 2008; non-marine ions Fe, Mn and $NH_4$ are neglected):

$$aNa^+ + bK^+ + cMg^{2+} + dCa - Exch \leftarrow\rightarrow dCa^{2+} + Na_aK_bMg_c - Exch \quad (16)$$

$$\text{with : } d = c + \tfrac{1}{2}(a+b)$$

$$BEX = Na + K + Mg - 1.0716\ Cl\ (meq/L) \quad (17)$$

Where: all ions in meq/L; 1.0716 = $[Na^+ + K^+ + Mg^{2+}]/Cl^-$ for AtOc.

Under the prevailing conditions, BEX is negative for seawater intrusion and positive for freshening. The magnitude of the exchange reaction in pure CNS is between −1 and −30 meq/L for all samples (24H330 excluded). As expected for seawater intrusion (Stuyfzand, 2008), the change in Ca concentration of infiltrated pure CNS (ΔCa) nearly equals -BEX (Fig. 5).

Sulfate in pure CNS shows a consistent, (very) small decrease between 0.6 and 2.9 mmol/L for all samples (excl. the 2 samples with 35 % dune water admixing). The corresponding concentration change of DIC (ΔDIC) is related to the $SO_4$ concentration change ($\Delta SO_4$) according to $\Delta DIC = -1.19\ \Delta SO_4$ (Fig. 5 Right). This value is close to the theoretical $\Delta DIC/\Delta SO_4$ ratio of −1.38 due to $SO_4$ reduction by SOM combined with pyrite formation, reductive dissolution of iron (hydr)oxides and calcite precipitation, according to the following equation:

$$2SO_4 + Fe(OH)_3 + 3.75\,CH_2O + Ca \rightarrow FeS_2 + CaCO_3 + 2\,HCO_3 + 0.75\,CO_2 + 4.25\,H_2O \quad (18)$$

Replacing $CH_2O$ by the Redfield equation ($CH_2O(NH_3)_{0.151}(H_3PO_4)_{0.0094}$; Froelich et al., 1979) yields a theoretical ΔDIC/ΔSO4 ratio of −1.07, which is also close to the observed ratio.

Compared to the northern transect, beyond 2–3 km from the HWL, the hydrochemical evolution along the southern transect shows less progress in the position of the intrusion front, and accordingly more cation exchange due to salinization (Ca and K in Fig. 4, lower BEX in Fig. 5 Left). Also, Fe and Mn (Fig. 4) are more mobilized, probably by combination of more manganous siderite dissolution and more desorption of $Fe^{2+}$ and $Mn^{2+}$. More interaction with aquitards in the southern transect (Fig. 3) partly explains the differences.

### 3.2. Trace elements

The results of trace elements are presented in Table 5, however, without the results of those parameters that were always below their minimum detection limit (MDL): Al (<4 μg/L), Be (<0.01 μg/L), Cd (<0.1 μg/L), Hg (<0.01 μg/L), rare earth elements (<0.01-<0.1 μg/L) and Th (<0.05 μg/L).

There are 6 groups of trace elements (TEs) displaying interesting, dissimilar behavior. The first is composed of Br and Sr which show more or less conservative behavior. Variations in their concentration are fully linked to variations in Cl concentration, on mg/L basis: Br = 3.492 $10^{-3}$ Cl ($R^2$ = 0.9996) and Sr = 4.216 $10^{-4}$ Cl ($R^2$ = 0.997). This is very close to the Br/Cl and Sr/Cl ratio in AtOc.

The second group is composed of F, B (Fig. 6), Li, Mo (Fig. 6) and Rb (Fig. 6), which show a concentration decrease downgradient, especially where passing aquitards. Russak et al. (2016) demonstrated that B and Li (and Mn) are adsorbed during salinization. The cations $Li^+$ and $Rb^+$ are likely sorbed mainly to negatively charged clay minerals (Rankama and Sahama, 1950), together with $K^+$ (Fig. 5). The anions $F^-$ and Mo (as $MoO_4^{2-}$) are either sorbed to positively charged iron (hydr)oxides (F: Bower and Hatcher, 1967; Mo: Rai and Zachara, 1984), or exchanging for OH in apatite (F: Sternitzke et al., 2012). Mo, after reduction to $Mo^{4+}$, is sorbed to negatively charged clay minerals or (co)precipitating as sulfide (Smedley and Kinniburgh, 2017). The uncharged B (as $H_3BO_3$) is known to be very susceptible to sorption by clay minerals (Parks and White, 1957; Keren and Muzeman, 1981). In basin aquifer recharge and deep well injection systems in the Dutch coastal dunes, this group behaves in a similar way (Stuyfzand, 2015). There, the infiltrated Rhine water with relative high concentrations is displacing ambient dune groundwater with much lower concentrations. This is similar to CNS water displacing less saline Holocene transgression water. The plots of B, Mo and Rb in Fig. 6 reveal 2 groups of data in the northern transect only: with relatively high (1) and low (2) concentrations. Fig. 8 shows that group 1 is associated with high $^{14}C$ activity (low age) and group 2 with low $^{14}C$ activity (high age).

Barium ($Ba^{2+}$), the only member of group 3, is characterized by a substantial mobilization from the aquifer system, in all samples. In theory, barite ($BaSO_4$) cannot be the Ba source, because coastal North Sea water is already supersaturated with respect to barite ($SI_B$ = 0.28), and the infiltrated North Sea water is even more supersaturated ($SI_B$ = 0.56–1.14). However, Verbruggen et al. (2020) demonstrated the

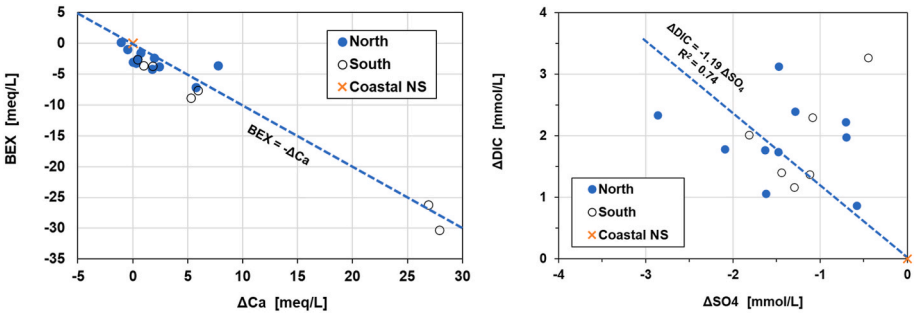


**Fig. 5.** BEX-ΔCa relation (Left) and ΔDIC-$\Delta SO_4$ relation (Right) for the samples of pure infiltrated CNS. Data corrected for dune water admixing.

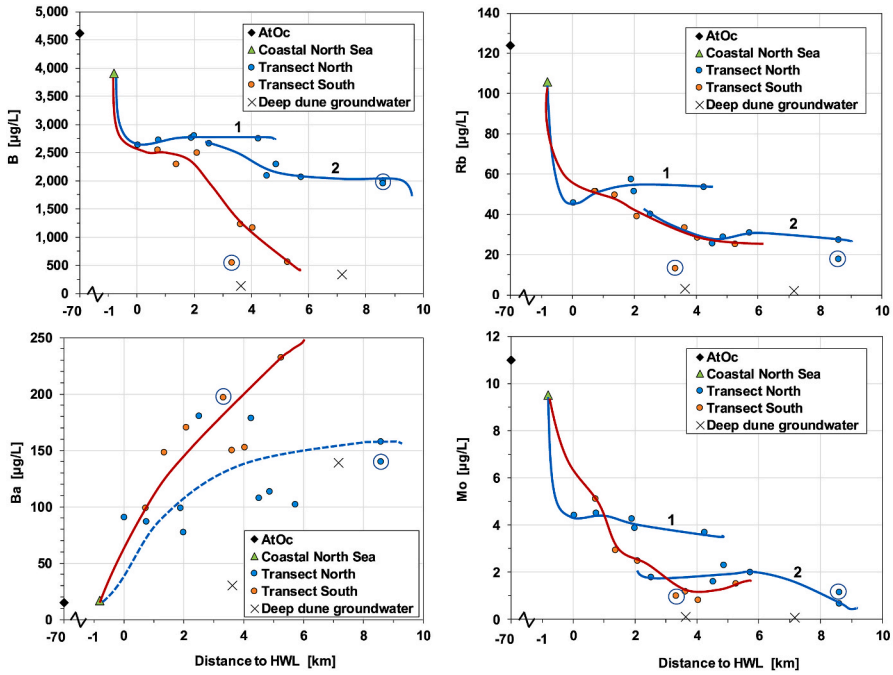


**Fig. 6.** Trace element changes of North Sea water down the hydraulic gradient, at 90–170 m BSL in semiconfined sand aquifer, moving towards the Haarlemmermeer polder. Based on data in Table 3. The 2 encircled data points indicate substantial admixing of fresh dune groundwater (ca. 35 %). HWL = High Water Line North Sea. 1 = relatively young group (1300–2200 y); 2 = relatively ancient group (3300–6600 y).

presence of ultrafine barite particles in 0.45 µm filtered water samples. Especially the passage of aquitards could provide ultrafine barite particles. Barite has not been used during well drilling operations. Other potential Ba sources are desorption (Russak et al., 2016), iron (hydr) oxides associated with marine diatoms (Sternberg et al., 2005), and shells (Fröhlich et al., 2023). The contribution of iron (hydr)oxides and shells is probably very small, because fresh dune groundwater passing Holocene marine clay layers rich in diatoms and shells does not show substantial Ba increases (Stuyfzand, 1993b).

The fourth group consists of As (as $AsO_4^{3-}$ and $H_3AsO_3$), $Co^{2+}$, $Ni^{2+}$ and $Zn^{2+}$, all of which show a (slightly) raised concentration in just 2 samples: 24H716 and 24H1331. The combined anomaly points at pyrite oxidation (Stuyfzand, 2015; Stuyfzand and Bonte, 2023), although the penetration of $O_2$ or $NO_3$ via the deep flow path seems impossible. Yet, there are 2 potential explanations. Firstly, a slow but protracted leakage-in of shallow, aerobic, fresh groundwater via shallow leaks in the PVC riser (Stuyfzand, 1983, 1993b; Lebbe et al., 1989). This is, however, contradicted by the lack of tritium (<0.03 TU). Secondly and more likely, ultrafine pyrite particles from the aquifer could have passed through the 0.45 µm filter, as the barite particles probably did (see above).

The fifth group shows elevated concentrations of Cu (as $Cu^+$ and $Cu^{2+}$), $Pb^{2+}$ and $Zn^{2+}$ in wells 24H287 and 25C8 only. Their riser and well screen are composed of cast-iron and brass, respectively, contrary to the other wells (all in PVC). The anomaly is thus produced by corrosion of the well screen.

The last group is composed of Se (as $SeO_4^{2-}$ and $SeO_3^{2-}$), U (as $UO_2^{2+}$ and $U^{4+}$) and V (as $VO_4^{3-}$, $VO^{2+}$ and $V(OH)_3$). In all samples, their concentration is substantially lower than in CNS. The retention mechanism probably consists of sorption to positively charged iron (hydr) oxides, and U (also) by precipitation as $UO_2$ at the onset of $SO_4$ reduction (Stuyfzand 1984).

### 3.3. Isotopes

Analytical results (Table 6) of the stable water isotopes $^2H$ and $^{18}O$ (Fig. 7) show that CNS and the 18 samples of CNS infiltrate are a mixture of AtOc water with river water (mainly Rhine).The Cl – $\delta^{18}O$ plot distinguishes the samples dominated by river water mixing from the ones dominated by dune groundwater mixing (see also section 3.1). The relation of $^{18}O$ with distance to the HWL (Fig. 8) strongly resembles the Cl-HWL relation in Fig. 4, as expected.

The relation of $^{14}C_{DIC}$ with distance to the HWL (Fig. 8) shows 2 groups of data in the northern transect. Group 1 is associated with high

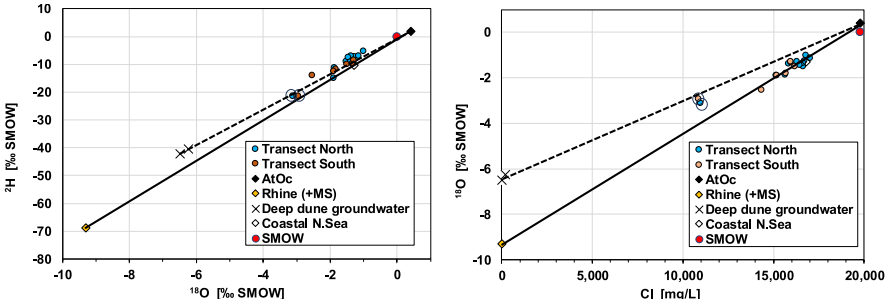


**Fig. 7.** Relation between $\delta^2H$ and $\delta^{18}O$, and $\delta^{18}O$ and Cl for the 18 groundwater samples and end members AtOc, coastal North Sea, Rhine River and fresh deep dune groundwater.

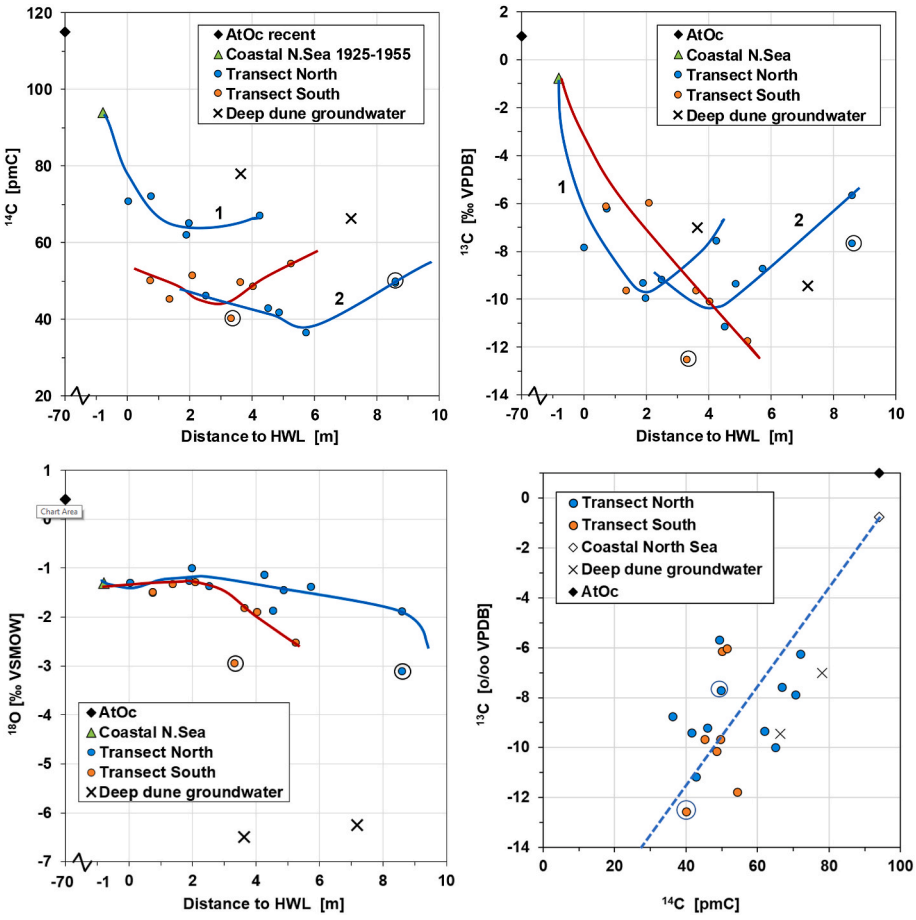


**Fig. 8.** Concentration of $^{14}C$, $\delta^{13}C$ and $\delta^{18}O$ as function of distance to the current North Sea High Water Line (HWL), and the relation between $\delta^{13}C$ and $^{14}C$, for saline groundwater samples taken below the fresh dune water lens in 2022. Only the encircled samples contain a substantial amount of admixed fresh dune groundwater (35 %); 1 = relatively young group (0.37–1,92 y); 2 = relatively ancient group (3300–6600 y).

$^{14}C$, relatively short distance to HWL, and high concentrations of B, Mo and Rb (Fig. 6), and group 2 with low $^{14}C$ (high age), a longer distance to HWL, and low concentrations of B, Mo and Rb (Fig. 6). Samples along the southern transect are closer to group 2 than to group 1.

The $\delta^{13}C_{DIC}$ values decrease prominently with distance to the HWL along the southern transect (Fig. 8). For both transects $\delta^{13}C_{DIC}$ values decrease with decreasing $^{14}C$ concentration. This indicates that reactions of CNS with sediment organic material and carbonates become increasingly important along the flow path.

All samples of CNS infiltrate are practically without tritium ($^{3}H$ < 0.03 TU), indicating that they do not contain a measurable fraction of subrecent (<70 years old) CNS or dune water.

### 3.4. Reaction scheme

The sample composition has been corrected for the contribution of admixed dune groundwater, to reserve the reaction scheme for pure CNS water. The reaction scheme is based on the confirmed presence of reactive mineral phases (Table 1) and consistent with the mineral saturation index ($SI_M$) of the water samples. The $SI_M$'s show quasi-equilibrium (0 ± 0.3) with calcite, dolomite and siderite, and strong undersaturation regarding among others halite and gypsum (Table 6). Halite and gypsum are indeed not present in the aquifer system.

The order of mineral encounter is important (Freeze and Cherry, 1979). For the $\delta^{13}C$ balance it is paramount to take into account the initial dissolution and later precipitation of calcite. For the $^{14}C$-dating it is crucial to know the age of the dissolving carbonates and oxidizing Sediment Organic Matter (SOM). The reaction scheme along the flow path of intruding CNS is based on Stuyfzand (1993b). Firstly, $O_2$ and $NO_3$ are reduced by SOM in seafloor sediment with some $CaCO_3$ dissolution by the $CO_2$ produced. In the Holocene aquitard A, $Fe(OH)_3$ and a small fraction of $SO_4$ are reduced by SOM with ensuing pyrite formation and $CaCO_3$ precipitation, while the dissolution of opaline diatoms and foraminifera leads to most of the $SiO_2$ increase. In aquitards C-E and further downgradient, cations are exchanged, some $CaCO_3$ precipitates due to Na, K and/or Mg expelling Ca from the exchanging phases, and siderite ($FeCO_3$) is dissolved.

Salinization in a near-neutral aquifer is generally accompanied initially by $CaHCO_3^+$ desorption leading to alkalinization, followed by proton buffering leading to acidification (Griffioen, 1993). These reactions can be schematized e.g. as follows:

$$\text{Alkalinization} \quad CaHCO_3 - X + \tfrac{1}{2}Ca^{2+} \leftarrow\rightarrow \tfrac{1}{2}Ca - X + Ca^{2+} + HCO_3^- \tag{19}$$

$$\text{Proton buffering} \quad H - X + \tfrac{1}{2}Ca^{2+} + HCO_3^- \leftarrow\rightarrow \tfrac{1}{2}Ca - X + CO_2 + H_2O \tag{20}$$

Alkalinization (Eq. (19) to right) raises TDS somewhat and takes only place when the Na–Ca exchange is peaking during the first phase of cation exchange. Proton-buffering (Eq. (20) to right) slightly reduces TDS, starts after the maximum of Na–Ca exchange, and lasts much longer. The position of the intrusion front and BEX data suggest that all samples were taken after the maximum of Na–Ca exchange, so that we only consider proton-buffering. Based on data in Griffioen (1993), we estimate the magnitude of $CO_2$ production $\Delta CO_2 = 0.04\ HCO3_{CNS}$.

The reaction equations are presented in Table 3, those with SOM in

more elaborated form (including $NH_3$ and $H_3PO_4$ as part of SOM) in A1. Inclusion of $NH_3$ and $H_3PO_4$ is needed because they impact on DIC speciation. Their most likely contribution varies between the Redfield equation ($CH_2O(NH_3)_{0.151}(H_3PO_4)_{0.0094}$; Froelich et al., 1979) and the marine SOM composition proposed by Hartmann et al. (1973): $CH_2O(NH_3)_{0.075}(H_3PO_4)_{0.0045}$. The Redfield equation is taken as standard here.

Methane forms an important gas, because it is generally accompanied by $CO_2$, $NH_4$, $PO_4$, DOC, and a relatively high $^{13}C$ content of the $CO_2$ (Stuyfzand 1994; Stuyfzand and Bonte, 2023). Its analysis is, however, often (also here) overlooked and therefore a crude estimate is warranted. In the reaction scheme, its production is coupled to the magnitude of $SO_4$ reduction, with default $CH_4 = -0.025\ \Delta SO_4$ (if $\Delta SO_4 < 0$, else $CH_4 = 0$).

### 3.5. The chemical mass balance

An example of the chemical mass balance (CMB) for the main constituents and the interlinked CMB for carbon isotopes is presented and discussed in A2. The perfect CMB would show a perfect match between the modeled and measured $HCO_3$ and $\delta^{13}C_{DIC}$. The calibration and fine-tuning process is described in A2. Most samples display an excellent fit for the main calibration parameters $HCO_3$ and $\delta^{13}C_{DIC}$. Their balance only failed for sample 25C12-128.

Table 7 shows the results of mass balancing the main constituents and $\delta^{13}C_{DIC}$ for all 18 samples of pure CNS infiltrate. The results include the mass transfer between the reactive solids and water, and the contribution of each endmember to the mixed water sample.

Good relations between the parameters in Table 7 are found for $\Delta FeS_2$, $\Delta Fe(OH)_3$, $\Delta CH_2O$ and $\Delta CaCO_3$ (Fig. A4). This is due to the dominance of reaction equation (18), composed of $SO_4$ reduction by SOM, followed by precipitation of the formed S as $FeS_2$, which requires at least an equal amount of (i) $Fe(OH)_3$ reduction by SOM and (ii) $CaCO_3$ precipitation. These combined reactions explain the high $r^2$ value in Fig. A4, but the theoretically expected slope according to Eq. (18) deviates substantially from the portrayed CMB slope for the relations with $\Delta CaCO_3$.The additional $CaCO_3$ change is largely dictated by cation exchange, which augments the $CaCO_3$ precipitation, because on average Na, K and Mg are expelling Ca from the exchanger.

Along both transects, ΔExch-C (half the sum of all main cations involved in exchange) shows effects of a longer distance to HWL (Table 7). This is explained by the advancement of the S/L intrusion front (Fig. 2). Additionally, along the southern transect, there is an increase for $\Delta CaCO_3$ and $\Delta FeCO_3$ up to ca. 4 km distance, and an increase of $\delta^{13}C_{DIC}$ and $HCO_3$.

### 3.6. Radiocarbon age dating

Table 8 shows the results of $^{14}C_{DIC}$ analysis of all 18 samples of CNS infiltrate, without ($^{14}C_M$) and with corrections ($^{14}C_{M+C}$) for the admixing of dune groundwater and for the 72 years between sampling and lab standard reporting year 1950. The age was calculated using $^{14}C$ models A-D, based on Eqs.(13)–(15). The model D ages, which are considered the more accurate, vary for all samples between 0.37 and 6 ka (disregarding the anomalous value of 9854 ka for sample 24H1325-123). The conventional ages are on average 1.7 times higher than model D ages, model B ages 1.3 times, and model C ages 1.07 times.

Table 8 also presents the $^{14}C_{ND}$, which is the calculated $^{14}C_{DIC}$ with the diluting effects of carbonate mineral dissolution and SOM oxidation, but without decay. The spatial distribution of the $^{14}C$-model D ages is shown along both transects in Fig. 9, and in planar view on the aquifer system in Fig. 10. Relatively low ages (<3 ka) are only found along the northern transect, in zone a (Fig. 10). All other wells show ages between 3 and 6 ka, most of which in zone 'b' (3–5 ka) and the remainder in zone 'c' (5–6 ka).

The age pattern in Fig. 10 is explained as follows. The sampled CNS

**Table 7**
Results of chemical mass balancing 18 saline groundwater samples, after correction for admixed dune groundwater (see also Fig. A1). $f_D$, $f_R$, $f_O$ = fraction of dune groundwater, river water and Atlantic Ocean water in mixed sample; ## = mass transfer (positive = solution enriched; negative = solution depleted) by pyrite, siderite, iron (hydr)oxide, manganous oxide, calcite, sed. organic material, (mainly) amorphous silica and cation exchange, respectively. Calibration results for $HCO_3$ and $\delta^{13}C_{DIC}$ (measured versus calculated by model) with the Root Mean Square Error (RMSE; definition in footnote).

| Sample | depth | X-HWL | $f_D$ | $f_R$ | $f_O$ | $FeS_2$ | $FeCO_3$ | $Fe(OH)_3$ | $MnO_2$ | $CaCO_3$ | $CH_2O$ | $SiO_2$ | Exch-C | $^{13}C_{MEAS}$ | $^{13}C_{CALC}$ | $HCO_3$-m | $HCO_3$-c | RMSE |
|---|---|---|---|---|---|---|---|---|---|---|---|---|---|---|---|---|---|---|
| Well code | m ASL | km | End-members of mix | | | mmol/L ## | | | | | | | meq/L | ‰VPDB | | mmol/L | | |
| 24H287 | -84 | 0.04 | 0.030 | 0.147 | 0.823 | -0.24 | 0.14 | 0.34 | 0.01 | -0.48 | 1.24 | 0.07 | 1.24 | -7.92 | -7.92 | 2.85 | 2.85 | 0.00 |
| 24H597 | -100 | 0.76 | 0.009 | 0.150 | 0.840 | -0.37 | 0.36 | 0.37 | 0.01 | -0.84 | 1.83 | 0.09 | 2.65 | -6.24 | -6.30 | 3.19 | 2.94 | 0.18 |
| 24H473 | -171 | 1.91 | 0.000 | 0.156 | 0.844 | -0.49 | -0.22 | 0.69 | 0.01 | -0.39 | 2.40 | 0.11 | 1.56 | -9.34 | -9.43 | 3.84 | 3.67 | 0.14 |
| 24H507 | -133 | 2.00 | 0.000 | 0.151 | 0.849 | -0.29 | -0.07 | 0.37 | 0.01 | 0.10 | 1.42 | 0.11 | 2.53 | -10.00 | -10.00 | 3.77 | 3.77 | 0.00 |
| 24H716 | -112 | 2.53 | 0.009 | 0.150 | 0.840 | -0.24 | -0.10 | 0.33 | 0.01 | 0.44 | 1.32 | 0.11 | 3.80 | -9.22 | -10.03 | 5.05 | 4.20 | 0.83 |
| 24H330 | -120 | 4.26 | 0.000 | 0.140 | 0.860 | -0.03 | -0.04 | 0.04 | 0.01 | 0.65 | 0.43 | 0.10 | 2.95 | -7.58 | -7.89 | 4.26 | 3.60 | 0.52 |
| 24H332 | -183 | 4.54 | 0.000 | 0.208 | 0.792 | -0.17 | 0.06 | 0.17 | 0.01 | 0.62 | 0.94 | 0.18 | 3.17 | -11.17 | -11.17 | 4.38 | 4.38 | 0.00 |
| 25C8 | -134 | 4.88 | 0.020 | 0.149 | 0.831 | -0.73 | 0.42 | 0.73 | 0.01 | -1.32 | 3.37 | 0.12 | 4.50 | -9.40 | -9.42 | 3.83 | 3.78 | 0.04 |
| 25C332 | -135 | 5.75 | 0.057 | 0.143 | 0.799 | -0.48 | 0.44 | 0.48 | 0.01 | -0.99 | 2.33 | 0.10 | 4.06 | -8.71 | -8.90 | 4.00 | 3.36 | 0.48 |
| 25C12 | -165 | 8.61 | 0.098 | 0.137 | 0.765 | -0.17 | 0.49 | 0.17 | 0.01 | 0.14 | 1.02 | 0.17 | 5.86 | -5.28 | -5.28 | 4.40 | 4.40 | 0.00 |
| 25C12 | -128 | 8.61 | 0.348 | 0.099 | 0.553 | -0.11 | 0.49 | 0.11 | 0.01 | -0.05 | 0.71 | 0.05 | 12.16 | *-6.78* | *-4.26* | *5.82* | *3.59* | 2.38 |
| 24H1331 | -94 | 0.75 | 0.035 | 0.146 | 0.818 | -0.15 | -0.12 | 0.19 | 0.01 | 0.09 | 0.94 | 0.08 | 3.05 | -6.11 | -6.23 | 3.30 | 2.94 | 0.27 |
| 24H1248 | -93 | 1.38 | 0.050 | 0.144 | 0.805 | -0.51 | 0.17 | 0.71 | 0.02 | -0.90 | 2.41 | 0.10 | 3.50 | -9.81 | -9.81 | 3.50 | 3.50 | 0.00 |
| 24H1305 | -113 | 2.10 | 0.049 | 0.144 | 0.807 | -0.43 | 0.41 | 0.43 | 0.02 | -1.08 | 2.09 | 0.09 | 4.22 | -5.97 | -6.09 | 3.44 | 2.85 | 0.43 |
| 24H1325 | -123 | 3.34 | 0.353 | 0.098 | 0.549 | -1.51 | 0.59 | 1.52 | 0.04 | -2.04 | 6.62 | -0.04 | 32.07 | -15.61 | -15.61 | 6.29 | 6.29 | 0.00 |
| 24H750 | -112 | 3.64 | 0.065 | 0.142 | 0.793 | -1.01 | 0.74 | 1.01 | 0.03 | -2.33 | 4.53 | 0.15 | 10.05 | -9.85 | -9.92 | 3.87 | 3.71 | 0.12 |
| 24H718 | -114 | 4.05 | 0.094 | 0.138 | 0.768 | -0.04 | 0.21 | 0.04 | 0.03 | 0.57 | 0.49 | 0.10 | 6.01 | -10.47 | -10.52 | 4.10 | 4.00 | 0.08 |
| 24H607 | -123 | 5.27 | 0.144 | 0.130 | 0.726 | -0.20 | 0.09 | 0.20 | 0.04 | 0.77 | 1.13 | 0.08 | 26.11 | -12.59 | -12.59 | 4.90 | 4.90 | 0.00 |
| Mean North | -133 | 3.53 | 0.022 | 0.153 | 0.825 | -0.32 | 0.15 | 0.37 | 0.01 | -0.21 | 1.63 | 0.11 | 3.2 | -8.49 | -8.6 | 4.0 | 3.69 | 0.22 |
| Mean South | -108 | 2.86 | 0.073 | 0.141 | 0.786 | -0.39 | 0.25 | 0.43 | 0.02 | -0.48 | 1.93 | 0.10 | 8.8 | -9.13 | -9.2 | 3.9 | 3.65 | 0.15 |

Exch-C = 0.5 x meq/L sum of all main cations involved in exchange process.

RMSE = $\mathrm{sqrt}\{[(HCO3_M\text{-}HCO3_C)^2+(^{13}C_M\text{-}^{13}C_C)^2]/2\}$

**Table 8**
Results of $^{14}C$ age dating of sampled saline groundwater. In the $^{14}C_{DIC}$ columns: m = as measured in 2022; m + c = as measured but corrected for admixing of dune groundwater and for the 72 years between sampling and lab standard reporting year 1950; ND = calculated model D activity based on CNS input of 91.68 pmC and diluting reactions, but No Decay (see Eq. (15)); In the $^{14}C$ Age columns: Conv. = conventional age assuming $^{14}C_{ND}$ = 100 pmC; Model B = age assuming $14C_{ND}$ = 91.68 pmC; Model C, D = calculated age using Eqs. (14) and (15) for $^{14}C_{ND}$, respectively, both with $^{14}C_{MEAS}$ = $^{14}C$ m + c. Anomalous values in italics.

| Sample | depth | X-HWL | $^{14}C_{DIC}$ [pmC] | | | $^{14}C$ Age [year] | | | |
|---|---|---|---|---|---|---|---|---|---|
| Well code | m ASL | km | m | m+c | ND | Conv. | Model B | Model C | Model D |
| 24H287 | -84 | 0.04 | 71.2 | 70.4 | 81.9 | 2906 | 2187 | 1777 | 1022 |
| 24H597 | -100 | 0.76 | 72.6 | 71.9 | 77.8 | 2730 | 2012 | 1276 | 365 |
| 24H473 | -171 | 1.91 | 62.5 | 62.0 | 81.2 | 3959 | 3241 | 1801 | 1924 |
| 24H507 | -133 | 2.00 | 65.5 | 64.9 | 83.2 | 3571 | 2853 | 1448 | 1828 |
| 24H716 | -112 | 2.53 | 46.4 | 45.7 | 81.5 | 6483 | 5764 | 3496 | 4592 |
| 24H330 | -120 | 4.26 | 67.4 | 66.9 | 80.2 | 3330 | 2611 | 854 | 1403 |
| 24H332 | -183 | 4.54 | 43.2 | 42.8 | 77.9 | 7021 | 6303 | 4468 | 4785 |
| 25C8 | -134 | 4.88 | 42.0 | 41.1 | 74.0 | 7354 | 6635 | 5305 | 4470 |
| 25C332 | -135 | 5.75 | 36.6 | 34.5 | 73.4 | 8801 | 8083 | 6753 | 5903 |
| 25C12 | -165 | 8.61 | 49.7 | 47.5 | 71.8 | 6159 | 5440 | 3930 | 3218 |
| 25C12 | -128 | 8.61 | 50.2 | 41.2 | 73.4 | 7336 | 6618 | 4549 | 4600 |
| 24H1331 | -94 | 0.75 | 50.5 | 49.1 | 87.2 | 5881 | 5162 | 4434 | 4572 |
| 24H1248 | -93 | 1.38 | 45.6 | 43.5 | 77.0 | 6878 | 6160 | 5246 | 4392 |
| 24H1305 | -113 | 2.10 | 51.8 | 50.1 | 77.0 | 5724 | 5005 | 4118 | 3247 |
| 24H1325 | -123 | 3.34 | 40.4 | *19.8* | 69.3 | *13402* | *12684* | *9839* | *9854* |
| 24H750 | -112 | 3.64 | 50.0 | 47.7 | 71.4 | 6128 | 5410 | 3996 | 2984 |
| 24H718 | -114 | 4.05 | 48.9 | 45.5 | 79.8 | 6519 | 5801 | 4236 | 4526 |
| 24H607 | -123 | 5.27 | 54.8 | 50.4 | 76.5 | 5660 | 4942 | 2789 | 3278 |
| Mean North | -133 | 3.53 | 55.7 | 54.8 | 78.3 | 5231 | 4263 | 2876 | 2951 |
| Mean South | -108 | 2.86 | 50.3 | 47.7 | 78.1 | 6132 | 5402 | 4139 | 3833 |

with ages greater than 3 ka intruded in the period 5–3 ka BP in an open coastal sea environment (Zagwijn, 1974; Vos et al., 2020) driven by vertical and lateral density differences. The intrusion happened in front of beach barriers that successively expanded westward (Fig. A7). This CNS infiltrate was probably mixed by the dynamics arising from density driven flow, and by subsequent dispersion and diffusion within the aquifers during (semi)stagnant conditions for several millennia. After 3 ka BP a different seawater intrusion mechanism became dominant. Rather than being driven by vertical density gradients it formed by the circulatory flow of intruded seawater beneath the freshwater lens (Jiao and Post, 2019). The reclamation of Lake Haarlemmermeer in 1850 and groundwater extraction since 1853 have accelerated the intrusion of seawater. This might be the reason why zone 'a' has a remarkable shape with a finger pointing inland (Fig. 10), towards the focus area of dune groundwater extraction in the period 1853–1980. Other factors cannot be ruled out, however. For instance, gaps in aquitards A and C could be present offshore, and higher permeability sand in aquifers 2 and 3 could prevail along the finger.

Zone 'a' is not present along the southern part of the coastline, probably due to a combination of factors: In the south, the coastline 2 ka ago extended further seaward (Fig. A7), the hydraulic conductivity of the aquifer sands is possibly lower, and/or the vertical hydraulic resistance of offshore aquitards A and C is possibly higher. A higher resistance leads to a longer vertical travel time, longer freshwater tongues that need to be bypassed, and a reduced hydraulic gradient in the underlying aquifers due to head losses in the aquitards above and due to the longer distance between the seaward point of the freshwater tongue and inland exfiltration point. Fig. 10 shows that zone 'c' partly coincides with the extension of glaciolimnic clay (aquitard B).

Sources of uncertainty in the presented $^{14}C$ model D ages mainly consist of estimates of the following parameters: the average $^{14}C$ activity (age) of $CaCO_3$ and SOM in the (sub)recent seafloor sediment ($^{14}C_{SEA-FLOOR}$) and in the Holocene sedimentary sequence below the seafloor ($^{14}C_{HOL}$), the average $^{13}C_{SOM}$ content, and the $^{14}C_{CNS}$ activity. A sensitivity analysis was therefore initiated looking for effects of varying the chosen four parameters on the $^{14}C$ model D age. The sensitivity analysis indicated that $^{14}C_{HOL}$ creates most uncertainty by far (A2), which is in line with the findings by Post (2004) for other parts of the Dutch coastal zone. The best parameter estimates are presented in Fig. A2.

### 3.7. Comparison with direct age simulation

Fig. 11 shows the simulated salinity distribution with the contour lines of the calculated direct age overlain for the year 2022. A full discussion of the evolution of the salinity and age distribution during the 3.5 ka simulation time is beyond the scope of this paper. The main thing to note is that the 3 ka direct age contour roughly forms a separation between the relatively young groundwater in zone a and the older (>3 ka) groundwater of zones b and c. The exceptions are the relatively young water from well 24H473 (which is found deeper than predicted by the model) and the relatively old water from well 24H716 (which, based on the model, should be much younger). These differences are explainable by the assumptions made in the model about the uniformity of the geology along the coast, projections of the samples onto the transect and possibly shore-parallel flow that is not captured by the 2D model. Overall though the direct age pattern is a reflection of the pattern

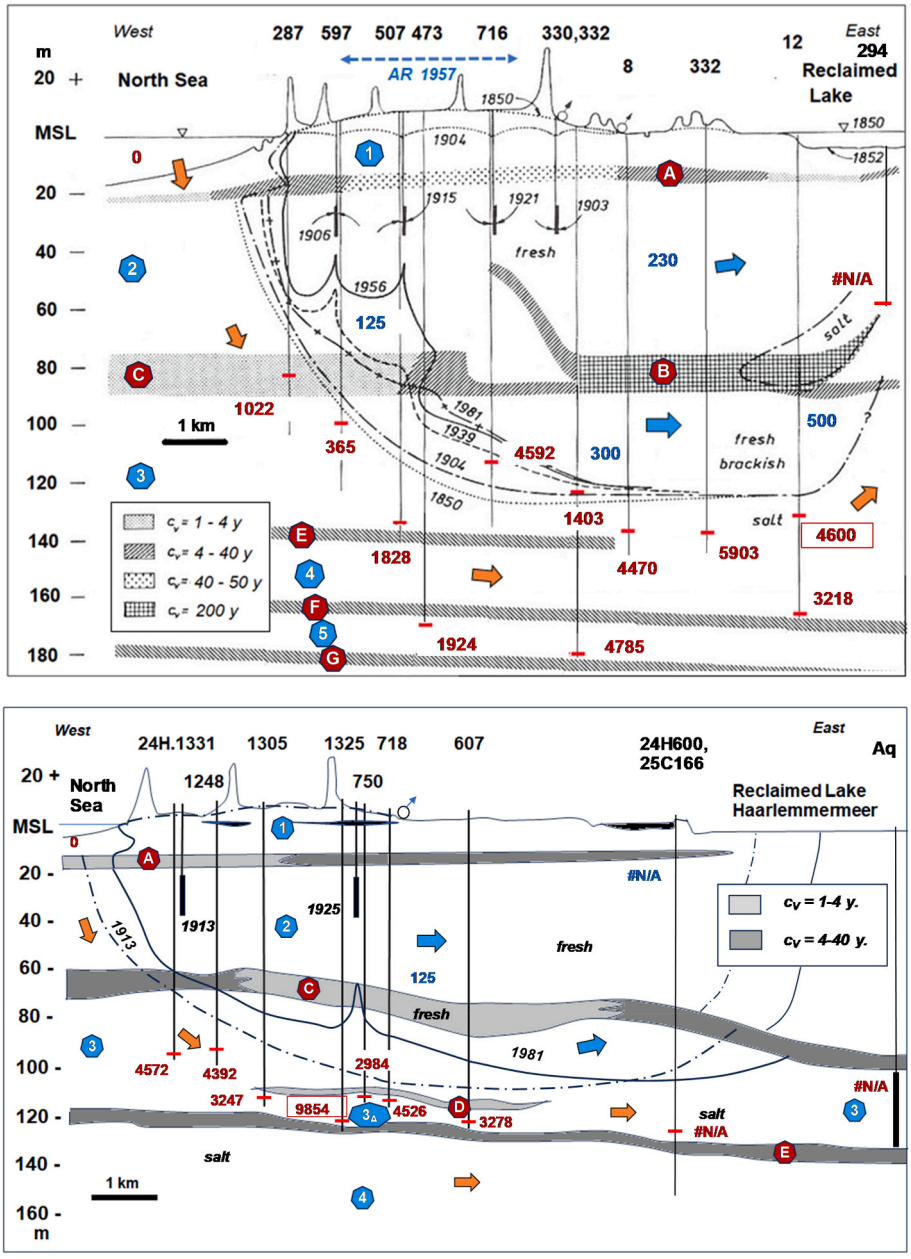


**Fig. 9.** Northern (top) and southern transect (bottom) with the $^{14}C$ model D age (years) of the intruded North Sea water in red. Numbers in blue = approximate age of fresh dune groundwater. 1–5 = aquifers, A – G = aquitards (see Table 1). The framed red numbers indicate substantial admixing of fresh dune groundwater (ca. 35 %), which was corrected for (as in all samples). Calendar age = $^{14}C$ age +72 year. (For interpretation of the references to color in this figure legend, the reader is referred to the Web version of this article.)

of the measured $^{14}C$ ages. This is encouraging given the complexity of the reaction scheme and the inherent assumptions.

### 3.8. Uncertainties and limitations

The observed groundwater quality patterns in this study are clear enough to quantify the processes through chemical mass balancing and $^{14}C$ age dating. However, various sources of uncertainty warrant some discussion. The following main sources of uncertainty are discerned.

The first regards the chemical and carbon isotopic mass balances, which are interrelated. No attempts have been made to look for alternative reaction schemes, because the results for 18 samples offer a coherent picture.

The second is related to the composition of intruding CNS water. It is assumed constant, even though the position and discharge of the main Rhine River outlets changed during the considered Holocene period. The Old Rhine outlet, situated 10–14 km southwest of the transects, was the main outlet in the period 6.5–1.9 ka BP (De Haas et al., 2019). It silted up in the period 100–800 AD, during which the outlet 35 km southwestward became the main outlet, which it is still today. Nevertheless, the CNS composition remained more or less constant, as evidenced by the Cl and $\delta^{18}O$ data for both the young and old CNS infiltrate (Fig. 7). The assumption that also $\delta^{13}C_{DIC}$ and $^{14}C_{DIC}$ in CNS remained constant is more uncertain, because data on (pre)historical Rhine River data are indirect and very scarce (Lanting & Van Der Plicht, 1998). Changing the $^{14}C_{DIC}$ in CNS from 91.7 to 94.0 pmC raises the age slightly (scenario D. III versus D.I in Table A3).

Last but not least, the $^{14}C$ age determination is most sensitive to the assumed $^{14}C$ activity (age) of the reactive carbonate minerals and sedimentary organic carbon in submarine Holocene deposits. The

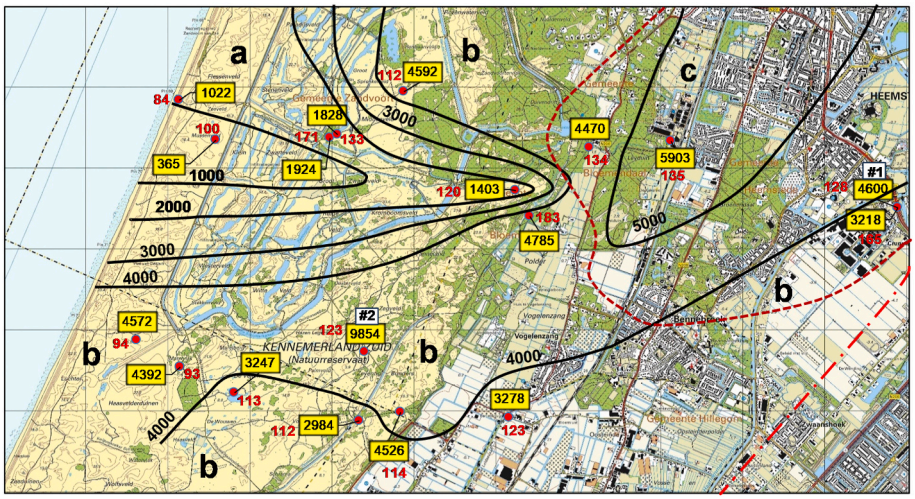


**Fig. 10.** Carbon-14 model D age (year) of infiltrated North Sea water (in yellow rectangle) in planar view on the aquifer at 80–180 m BSL. Zones: a = <2 ka; b = 3–5 ka; c = 5–6 ka. The dark red dashed line delimits the inside presence of aquitard B (glaciolimnic clay) on top of aquitard C (fluvial clay loam). The red dot stripe line marks the approximate position of the North Sea intrusion front (defined as the 10,000 mg Cl/L line). #1 = corrected for 35 % admixed dune groundwater; #2 = as #1 but considered an anomaly; red numbers = well screen depth in m BSL. Calendar age = $^{14}$C age +72 year. (For interpretation of the references to color in this figure legend, the reader is referred to the Web version of this article.)

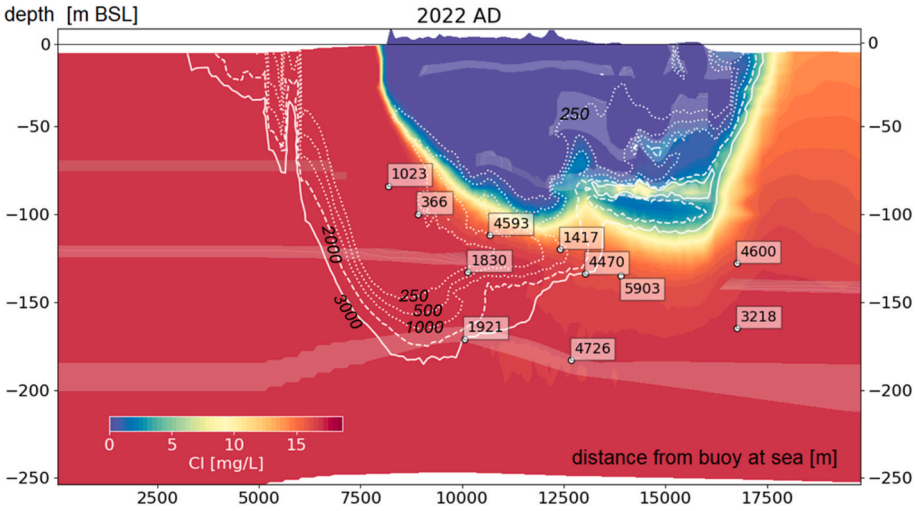


**Fig. 11.** Snapshot of the simulated salinity distribution along the northern transect, with the contour lines of the calculated direct age (numbers in italic; year) for the year 2022. Ages in rectangles represent the $^{14}$C model D ages (year) for each of the 11 monitoring well screens.

deeper Holocene deposits are more important than the seafloor deposits, because the dominant geochemical reaction consists of $SO_4$ and $Fe(OH)_3$ reduction, which is not taking place in the seafloor sands. The model D ages of CNS appear very sensitive to the $^{14}$C activity of the deeper Holocene deposits (scenarios D.V-D.VIII versus D.I in Table A2), but their spread (40–80 pmC) does not disturb the distinction between young (<3 ka) and old (3–6 ka) intruded CNS (Fig. A3).

These uncertainties limit the use of the calculated ages for calibrating the groundwater models that have been developed to manage the water supply system in the freshwater lens. At the same time the pronounced zonation in Fig. 10 has an important management implication. It challenges the widely-held assumption that flow patterns are more or less uniform along the coast. This means that the design and siting of underground activities (for example, deep aquifer storage and recovery systems) should take into account the increased susceptibility to salinization that this age pattern indicates.

## 4. Conclusions

This study aimed to quantify the age of North Sea water that is actively intruding into the coastal aquifers beneath the dune area of the Western Netherlands. CNS before and after infiltration has a uniform, recognizable Cl concentration of 16–17 g/L and a $\delta^{18}$O content of −1.3 ‰ V-SMOW. Based on these characteristics it could be established that CNS occupies the aquifers below the seafloor, below the freshwater lens down to at least 200 m BSL and about 2 km beyond the western border of reclaimed Lake Haarlemmermeer in the north and 1–2 km ahead of it in the south.

For each sample of intruded CNS a chemical mass balance was calculated, with a new Excel based code (R + SWi). The balance was corrected for the admixing of fresh dune groundwater. SOM oxidation is the dominant reaction according to the chemical mass balance, together with salinization induced cation exchange. The best of four tested radiocarbon dating methods is fully linked to the chemical mass balance, from which 11 reactions with a direct impact on carbon. It yields ages

between 0.3 and 6 ka, distributed in 2 main age zones: young (<3 ka) and old (3–6 ka) CNS. A sensitivity analysis revealed that the $^{14}C$ age determination is most sensitive to the assumed $^{14}C$ activity (age) of the reactive carbonate minerals and SOM in the submarine Holocene deposits.

The division between young and old CNS is consistent with the paleohydrology of the coastal area during the Holocene transgression, which was independently confirmed by simulation of age patterns using a numerical model. The spatial distribution of young CNS only in the north indicates a higher vulnerability to salinization. This study shows how radiocarbon data of intruding seawater strengthen the understanding of the hydrological processes of coastal aquifers.

## CRediT authorship contribution statement

**Pieter J. Stuyfzand:** Writing – review & editing, Writing – original draft, Visualization, Validation, Software, Methodology, Investigation, Formal analysis, Conceptualization. **Philip R. Nienhuis:** Writing – review & editing, Supervision, Resources, Project administration, Methodology, Funding acquisition, Data curation. **Vincent E.A. Post:** Writing – review & editing, Visualization, Validation, Methodology, Investigation, Formal analysis.

## Declaration of competing interest

The authors declare that they have no known competing financial interests or personal relationships that could have appeared to influence the work reported in this paper.

## Acknowledgements

This study was carried out by order of water utility Waternet (Amsterdam, Netherlands), within the framework of its hydrological research program (grant IDs 276397 and 720236), aiming at a.o., optimization of its 3D transient hydrological model AMWADU (based on Modflow) of the entire dune catchment area.

## Appendix A. Supplementary data

Supplementary data to this article can be found online at https://doi.org/10.1016/j.apgeochem.2025.106564.

## Data availability

The data that has been used is confidential.

## References

Bower, C.A., Hatcher, J.T., 1967. Adsorption of fluoride by soils and minerals. Soil Sci. 103, 151–154.

Clark, I.D., Fritz, P., 1997. Environmental Isotopes in Hydrogeology, 23. CRC Press, Taylor & Francis Group, Boca Raton, p. 328.

Currell, M.J., Dahlhaus, P., Hiroyuki, L., 2015. Stable isotopes as indicators of water and salinity sources in a southeast Australian coastal wetland: identifying relict marine water, and implications for future change. Hydrogeol. J. 23, 235–248. https://doi.org/10.1007/s10040-014-1199-9.

Dang, X., Gao, M., Wen, Z., Hou, G., Jakada, H., Ayejoto, D., Sun, Q., 2022. Saline groundwater evolution in the Luanhe River delta (China) during the Holocene: hydrochemical, isotopic, and sedimentary evidence. Hydrol. Earth Syst. Sci. 26, 1341–1356. https://doi.org/10.5194/hess-26-1341-2022.

De Haas, T., van der Valk, L., Cohen, K.M., et al., 2019. Long-term evolution of the old rhine estuary: unravelling effects of changing boundary conditions and inherited landscape. Deposition. Record 5, 84–108. https://doi.org/10.1002/dep2.56.

Delsman, J.R., Huang, K., Vos, P.C., de Louw, P.G.B., Oude Essink, G.H.P., Stuyfzand, P. J., Bierkens, M.F.P., 2014. Paleo-modeling of coastal saltwater intrusion during the Holocene: an application to the Netherlands. Hydrol. Earth Syst. Sci. 18, 3891–3905.

Domenico, P.A., Schwartz, F.W., 1998. Physical and chemical hydrogeology, 2nd ed. Wiley, p. 506p.

Freeze, R.A., Cherry, J.A., 1979. Groundwater, Prentice Hall Englewood Cliffs N.Y., p. 604.

Froelich, P.N., Klinkhammer, G.P., Bender, M.L., Luedtke, N.A., Heath, G.R., Cullen, D., Dauphin, P., Hammond, D., Hartman, B., Maynard, V., 1979. Early oxidation of organic matter in pelagic sediments of the eastern equatorial Atlantic : suboxic diagenesis. Geochim.et Cosmochim. Acta 43, 1075–1090.

Fröhlich, L., Siebert, V., Huang, Q., Thébault, J., Moriceau, B., Jochum, K.P., Schöne, B. R., 2023. Uptake of barium, molybdenum, and lithium and incorporation into scallop shells: refining proxies for primary production dynamics. Limnol. Oceanogr. 68 (11), 24–3590. https://doi.org/10.1002/lno.12440.

Goode, D.J., 1996. Direct simulation of groundwater age. Water Resour. Res. 32 (2), 289–296. https://doi.org/10.1029/95WR03401.

Griffioen, J., 1993. Multicomponent cation exchange including alkalinisation/acidification following flow through sandy sediment. Water Resour. Res. 29 (9), 3005–3019.

Harwood, A.J.P., Dennis, P.F., Marca, A.D., Pilling, G.M., Millner, R.S., 2008. The oxygen isotope composition of water masses within the north sea. Estuar. Coast Shelf Sci. 78 (2), 353–359. https://doi.org/10.1016/j.ecss.2007.12.010.

Haseguwa, T., Nakata, K., Tomioka, Y., Kondo, H., Kunimaru, T., Alexander, W.R., 2023. Modern and fossil seawater identification using ground- and pore-water dating from the western coast of the Miura Peninsula, Japan. Chem. Geol. 621, 121299. https://doi.org/10.1016/j.chemgeo.2022.121299.

Heaton, T.J., Köhler, P., Butzin, M., Bard, E., Reimer, R.W., Austin, W.E.N., Ramsey, C.B., Grootes, P.M., Hughen, K.A., Kromer B, B., et al., 2020. Marine20—the marine radiocarbon age calibration curve (0–55,000 cal BP). Radiocarbon 62, 779–820.

Jiao, J., Post, V., 2019. Coastal Hydrogeology. Cambridge Univ. Press, p. 403. https://doi.org/10.1017/9781139344142.007.

Kamps, P.W.T.J., Schaars, F.W., Olsthoorn, T.N., 2005. Calibration of the model of the amsterdam dune area using multiple stresses. Poster presented at ModelCare 2006, Scheveningen, June 2-6,, 2006.

Keren, R., Muzeman, V., 1981. Boron adsorption by clay minerals using a phenomenological equation. Clays Clay Miner. 29, 198–204.

Lanting, J.N., Van Der Plicht, J., 1998. Reservoir effects and apparent 14C-Ages. J. Irish Archaeol. 9, 151–165. http://www.jstor.org/stable/30001698.

Lebbe, L., Walraevens, K., Pede, K., 1989. Het probleem van lekkende peilbuizen bij de hydrogeologische studie van de Zwarte sluispolder. Water 46, 102–106.

Lee, S., Currell, M., Cendón, D.I., 2016. Marine water from mid-holocene sea level highstand trapped in a coastal aquifer: evidence from groundwater isotopes, and environmental significance. STOTEN 544, 995–1007. https://doi.org/10.1016/j.scitotenv.2015.12.014.

Molt, E.L., 1961. Verontreiniging van het rijnwater. 13e Vakantiecursus Drinkwatervoorziening, RID Leidschendam 46–71.

Mook, W.G., 1970. Stable carbon and oxygen isotopes of natural waters in the Netherlands. IAEA-SM-129/12. In: Isotope Hydrology 1970, Proc. Symp. Vienna, 9-13 March 1970, STI/PUB/255. IAEA Vienna, pp. 163–190.

Mook, W.G., 2005. Introduction to isotope hydrology. IAH-ICH Series - International Contributions to Hydrology. Balkema, p. 270. ISBN: 9780415381970.

Mook, W.G., van der Plicht, J., 1999. Reporting $^{14}C$ activities and concentrations. Radiocarbon 41 (3), 227–239.

Nienhuis, P.R., Olsthoorn, T.N., Kamps, P.T.W.J., 2014. Hydrological history of the amsterdam water supply dunes. Proc. SWIM 23, 265–268. Husum, Germany.

Nienhuis, P.R., Kamps, P.T.W.J., 2017. Generating initial fresh/saline groundwater distributions for a 3D ModFlow SWI model using cross-sectional seawat as a proxy. In: Proc. Modflow and More Conf, pp. 123–127. Golden, Colorado.

Parks, W.L., White, J.L., 1957. Boron retention by clay and humus systems saturated with various cations. Soil Sci. Soc. Am. Proc. 16, 298–300.

Plummer, P.D., Glynn, P., 2013. Radiocarbon Dating in Groundwater Systems. Ch.4 in IAEA Book "Isotope Methods for Dating Old Groundwater. IAEA Vienna, pp. 33–89.

Post, V.E.A., 2004. Groundwater Salinization Processes in the Coastal Area of the Netherlands due to Transgressions During the Holocene. Vrije Universiteit Amsterdam, p. 138p. PhD Thesis.

Rai, D., Zachara, J.M., 1984. Chemical attenuation rates, coefficients and constants in leachate migration; a critical review. ESPRI EA-3356 1 project 2198-1 final report.

Rankama, K., Sahama, T.G., 1950. Geochemistry. Univ. Chicago Press, p. 912p.

Russak, A., Sivan, O., Yechieli, Y., 2016. Trace elements (Li, B, Mn and Ba) as sensitive indicators for salinization and freshening events in coastal aquifers. Chem. Geol. 441, 35–46. https://doi.org/10.1016/j.chemgeo.2016.08.003.

Scourse, J.D., Wanamaker, A.D., Weidman, C., Heinemeier, J., Reimer, P.J., Butler, P.G., Witbaard, R., Richardson, C.A., 2012. The marine radiocarbon bomb pulse across the temperate north Atlantic: a compilation of $\Delta^{14}C$ time histories from arctica islandica growth increments. Radiocarbon 54 (2), 165–186.

Sivan, O., Yechieli, Y., Herut, B., Lazar, B., 2005. Geochemical evolution and timescale of seawater intrusion into the coastal aquifer of Israel. Geochem. Cosmochim. Acta 69 (3), 579–592. https://doi.org/10.1016/j.gca.2004.07.023.

Smedley, P.L., Kinniburgh, D.G., 2017. Molybdenum in natural waters: a review of occurrence, distributions and controls. Appl. Geochem. 84, 387–432. https://doi.org/10.1016/j.apgeochem.2017.05.008.

Sola, F., Fernandes-Cortes, A., Vallejos, A., 2025. Paleo-coastline reconstruction based on the hydrogeochemistry of coastal aquifers. Hydrogeol. J. https://doi.org/10.1007/s10040-025-02900-8.

Sternberg, E., Tang, D., Ho, T.Y., Jeandel, C., Morel, F.M.M., 2005. Barium uptake and adsorption in diatoms. Geochem. Cosmochim. Acta 69 (11), 2745–2752. https://doi.org/10.1016/j.gca.2004.11.026. ISSN 0016-7037.

Sternitzke, V., Kaegi, R., Audinot, J.N., Lewin, E., Hering, J.G., Johnson, C.A., 2012. Uptake of fluoride from aqueous solution on nano-sized hydroxyapatite: examination of a fluoridated surface layer. Environ. Sci. Technol. 46, 802–809. https://doi.org/10.1021/es202750t.

Stuyfzand, P.J., 1983. Important Sources of Error During Sampling Groundwater via Piezometers and Multilevel Miniscreens, pp. 87–94. H2O 16 (in Dutch).
Stuyfzand, P.J., 1988. Hydrochemie en hydrologie van duinen en aangrenzende polders tussen Noordwijk en Zandvoort aan Zee (kaartbladen 24H en 25C). KIWA-rapport SWE 87 (7), 343.
Stuyfzand, P.J., 1991. Trace elements in groundwater in the Netherlands. In: Dutch, $H_2O$ 24, pp. 20–25, 756-762 en $H_2O$ 25.
Stuyfzand, P.J., 1991c. Sporenelementen in Rijnoever-grondwater in het rivierengebied. Ch.8 in KIWA-Meded. 118, 129–154.
Stuyfzand, P.J., 1993a. Hydrochemistry and Hydrology of the Coastal Dune Area of the Western Netherlands. published by KIWA, p. 366. Ph.D. Thesis Vrije Univ. Amsterdam, ISBN 90-74741-01-0. http://dare.ubvu.vu.nl/handle/1871/12716.
Stuyfzand, P.J., 1993b. Behaviour of major and trace constituents in fresh and salt intrusion waters, in the Western Netherlands. In: Custodio, E., Galofré, A. (Eds.), Study and Modelling of Saltwater Intrusion into Aquifers, Proc. 12th Salt Water Intrusion Meeting, November 1992 Barcelona, CIHS. CIMNE Barcelona, pp. 143–160.
Stuyfzand, P.J., 2008. Base exchange indices as indicators of salinization or freshening of (coastal) aquifers. In: Program and Proceedings 20th Salt Water Intrusion Meeting, June 23-27, 2008, Naples (Fl) USA. Univ Florida, IFAS Research, pp. 262–265.
Stuyfzand, P.J., 2011. Hydrogeochemical processes during riverbank filtration and artificial recharge of polluted surface waters: zonation, identification and quantification. In: Ray, C., Shamrukh, M. (Eds.), Riverbank Filtration for Water Security in Desert Countries, Nato Science for Peace and Security Series C: Environmental Security, pp. 97–128.
Stuyfzand, P.J., 2012. Hydrogeochemcal (HGC 2.1), for Storage, Management, Control, Correction and Interpretation of Water Quality Data in Excel Spread Sheet. KWR Watercycle Research Institute, p. 96. KWR-report BTO.2012.244(s),updated in Dec. 2016.
Stuyfzand, P.J., 2015. Trace element patterns in Dutch coastal dunes after 50 years of artificial recharge with rhine river water. Environ. Earth Sci. 73 (12), 7833–7849. https://doi.org/10.1007/s12665-014-3770-z.
Stuyfzand, P.J., Stuurman, R.J., 2008. Origin, distribution and chemical mass balances for brackish and saline groundwaters in the Netherlands. In: Barrocu, G. (Ed.), Proc. 1st SWIM-swica Joint Saltwater Intrusion Conference. Cagliari-Baia de Chia, pp. 151–164. Sept24-29 2006.
Stuyfzand, P.J., Schaars, F., van der Made, K.J., 2011. Multitracing the origin of brackish and saline groundwaters near water catchment area monster. $H_2O$ (23), 34–37.
Stuyfzand, P.J., Bonte, M., 2023. A critical review of arsenic occurrence, fate and transport in natural and modified groundwater systems in the Netherlands. Appl. Geochem. 150 (2023), 18, 105596.
Van der Valk, L., 1992. Mid- and late-holocene Coastal Evolution in the beach-barrier Area of the Western Netherlands. Free Univ., Amsterdam, p. 235p. Ph.D. Thesis Inst. of Earth Sci.
Verbruggen, E.M.J., Smit, C.E., van Vlaardingen, P.L.A., 2020. Environmental quality standards for barium in surface water; proposal for an update according to the methodology of the water framework directive. RIVM-Letter Report 2020-0024. https://www.rivm.nl/bibliotheek/rapporten/2020-0024.pdf.
Vos, P.C., der Meulen, M., Weerts, H.J.T., Bazelmans, J., 2020. Atlas of the Holocene Netherlands; Landscape and Habitation Since the Last Ice Age. Amsterdam Univ. Press. ISBN 10: 9463724435, ISBN 13: 9789463724432.
Werner, A.D., Bakker, M., Post, V.E.A., Vandenbohede, A., Lu, C., Ataie-Ashtiani, B., Simmons, C.T., Barry, D.A., 2013. Seawater intrusion processes, investigation and management: recent advances and future challenges. Adv. Water Resour. 51, 3–26. https://doi.org/10.1016/j.advwatres.2012.03.004.
White, W.M., 2013. Geochemistry. Wiley Blackwell, p. 672.
Yechieli, Y., Sivan, O., Lazar, B., Vengosh, A., Ronen, D., Herut, B., 2001. Radiocarbon in seawater intruding into the Israeli mediterranean coastal aquifer. Radiocarbon 43 (2B), 773–781.
Yechieli, Y., Kafri, U., Sivan, O., 2009. The inter-relationship between coastal sub-aquifers and the Mediterranean Sea, deduced from radioactive isotopes analysis. Hydrogeol. J. 17, 265–274. https://doi.org/10.1007/s10040-008-0329-7.
Yechieli, Y., Yokochi, R., Zilberbrand, M., Lu, Z.-T., Purtschert, R., Sueltenfuss, J., Jiang, W., Zappala, J., Mueller, P., Bernier, R., Avrahamov, N., Adar, E., Talhami, F., Livshitz, Y., Burg, A., 2019. Recent seawater intrusion into deep aquifer determined by the radioactive noble-gas isotopes 81Kr and 39Ar. Earth Planet Sci. Lett. 507, 21–29. https://doi.org/10.1016/j.epsl.2018.11.028.
Zagwijn, W.H., 1974. The palaeogeographic evolution of the Netherlands during the Quaternary. Geol. Mijnbouw 53, 369–385.
Zuurdeeg, B.W., 1980. De natuurlijke chemische samenstelling van Maaswater. $H_2O$ 13, 2–7. https://edepot.wur.nl/391826.